JACS
JOURNAL OF THE AMERICAN CHEMICAL SOCIETY
pubs.acs.org/JACS
Article

Oxygen Reduction by Iron Porphyrins with Covalently Attached Pendent Phenol and Quinol

Asmita Singha, Arnab Mondal, Abhijit Nayek, Somdatta Ghosh Dey, and Abhishek Dey*

Cite This: https://dx.doi.org/10.1021/jacs.0c10385
Read Online

ABSTRACT: Phenols and quinols participate in both proton transfer and electron transfer processes in nature either in distinct elementary steps or in a concerted fashion. Recent investigations using synthetic heme/Cu models and iron porphyrins have indicated that phenols/quinols can react with both ferric superoxide and ferric peroxide intermediates formed during O_2 reduction through a proton coupled electron transfer (PCET) process as well as via hydrogen atom transfer (HAT). Oxygen reduction by iron porphyrins bearing covalently attached pendant phenol and quinol groups is investigated. The data show that both of these can electrochemically reduce O_2 selectively by $4e^-/4H^+$ to H_2O with very similar rates. However, the mechanism of the reaction, investigated both using heterogeneous electrochemistry and by trapping intermediates in organic solutions, can be either PCET or HAT and is governed by the thermodynamics of these intermediates involved. The results suggest that, while the reduction of the $Fe^{III}-O_2^{\cdot-}$ species to $Fe^{III}-OOH$ proceeds via PCET when a pendant phenol is present, it follows a HAT pathway with a pendant quinol. In the absence of the hydroxyl group the O_2 reduction proceeds via an electron transfer followed by proton transfer to the $Fe^{III}-O_2^{\cdot-}$ species. The hydrogen bonding from the pendant phenol group to $Fe^{III}-O_2^{\cdot-}$ and $Fe^{III}-OOH$ species provides a unique advantage to the PCET process by lowering the inner-sphere reorganization energy by limiting the elongation of the O−O bond upon reduction.

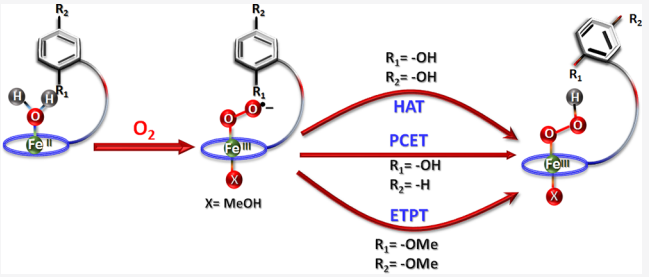

1. INTRODUCTION

Factors that can affect the rate and selectivity of the reduction of molecular oxygen are of great contemporary interest. In aerobic eukaryotes and higher animals, selective $4e^-/4H^+$ oxygen reduction is performed by the membrane-bound cytochrome C oxidase (CcO), which is a terminal oxidase in the respiratory redox chain in mitochondria.[1,2] The active site of CcO (Scheme 1a) is comprised of a histidine-bound heme a_3 and a histidine-ligated Cu_B center.[3] Of the three histidine residues, one is cross-linked with a tyrosine residue, which acts as an electron and proton donor during the reduction of oxygen in the case of a catalytically relevant mixed-valent (MV) state of heme-Cu oxidases.[4] The reduction of oxygen to water requires $4e^-$ and $4H^+$, and in the catalytic cycle of CcO out of the four electrons two are supplied by reduced heme a_3 (Fe^{II}), which is oxidized to ferryl (Fe^{IV}=O), one is supplied by Cu_B (Cu^I), which is oxidized to Cu^{II}, and the last electron is derived from the tyrosine residue, which is covalently attached to the His240 residue (Scheme 1a) through a post-translational modification, when the system is electron-deficient, that is, MV state, which avoids the formation of partially reduced oxygen species (PROS) like $O_2^{\cdot-}$ and OH·, which are detrimental to biological systems.[2,4−6,5−7] Several synthetic Fe-porphyrins and heme/Cu systems (Scheme 1b−d) have been reported, which can catalyze an electrochemical oxygen reduction both in an organic solvent as well as in an aqueous medium.[8,9] The unique post-translational modification has been emulated in synthetic heme/Cu systems (Scheme 1b,c) as well.[3] It has been observed that incorporation of Cu metal in the distal site of Fe-porphyrin not only produces a very stable ferric superoxide intermediate but also weakens the O−O bond enhancing the rate of its scission.[10,11] However, when the distance between Fe and Cu metal centers are flexible, addition of O_2 to the fully reduced heme/Cu complex results in the formation of a stable bridging $\eta^2:\eta^2$ Fe^{III}-peroxo-Cu^{II} species (Scheme 1b), where the peroxo ligand coordinates with Fe and Cu in either $\eta^2:\eta^2$ or $\eta^2:\eta^1$ fashion depending on the coordination number of the Cu center.[12−16] Inclusion of a phenol, either covalently attached to an imidazole or added externally, results in the formation of a phenoxyl radical akin to the Tyr244 radical formed in the active site of CcO (P_M state of CcO).[17,18] When these complexes are attached to an electrode and electrochemical oxygen reduction is investigated, these can selectively reduce oxygen to water even when the

Received: September 29, 2020

Scheme 1. Structures Investigated in This Work[a]

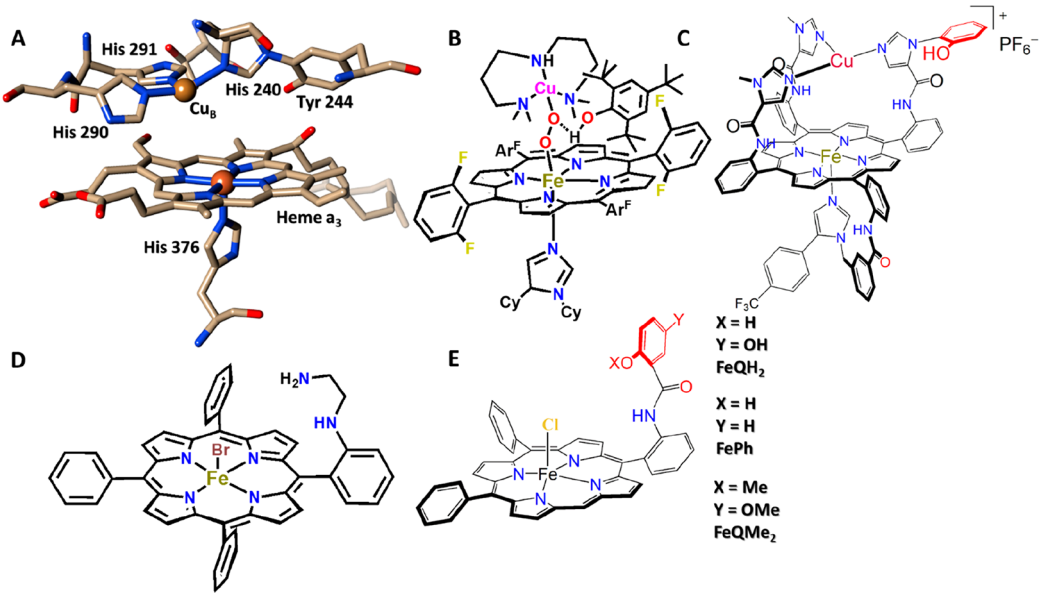

[a](A) Active site of CcO (truncated from pdb id: 2OCC). Schematic drawings of (B) proposed peroxide intermediate heme-Cu complex with external phenol. (C) Heme-Cu complex with a covalently attached phenol. (D) Fe porphyrin with a basic amine residue in the distal site and (E) Fe porphyrins having hydroquinone (FeQH$_2$), phenol (FePh), and 2,5-dimethoxy phenyl ring (FeQMe$_2$).

supply of electrons from the electrode is retarded (utilizing a self-assembled monolayer of thiol on Au electrodes), where the phenol donates an electron to oxygen to complete its 4e$^-$ reduction under these conditions mimicking the reactivity of the MV state of CcO.[19] Several recent investigations have highlighted the role of axial ligand and hydrogen bonding in these heme/Cu systems, with a particular focus on the factors that enable efficient scission of the peroxide bond, which is the last step of the reduction of oxygen to water, that is, cleaving the O−O bond.[20−24]

Electrochemical oxygen reduction being a multielectron multiproton process often results in the formation of PROS like O_2^- and H_2O_2 due to the incomplete reduction of oxygen.[25−28] In situ surface enhanced resonance Raman spectroscopy coupled to rotating disc electrochemistry (SERRS-RDE) on mononuclear Fe porphyrins having no discrete distal superstructure such as Fe-tetraphenyl porphyrin (FeTPP) show that the hydrolysis of an Fe^{III}−OOH intermediate is responsible for the release of H_2O_2 (Scheme 2).[29] The hydrolysis is accentuated when the electron transfer to this species is slow offering more time for this species to be hydrolyzed, and as much as 100% H_2O_2 can be detected when the electron transfer rate from the electrode to the immobilized iron porphyrin catalyst is slowed down to ∼10 s^{-1} using hexadecanethiol-coated Au electrodes.[27] The same peroxide intermediate is found to accumulate in iron porphyrins with a different axial ligand and in heme/Cu systems (both synthetic and biosynthetic) indicating that the cleavage of the O−O bond is the rate-determining step in ORR by iron porphyrins as well as heme/Cu systems under these conditions.[30−32] The pK_a of the proximal oxygen (bound to the iron) of the Fe^{III}−OOH intermediate is between 5.5 and 7.0 for neutral axial ligand and that of the distal oxygen (not bound to the iron) is about ∼1 unit lower.[33,34] Accordingly, spatial control of proton transfer directing it specifically to the distal oxygen of this Fe^{III}−OOH to affect a heterolytic O−O bond cleavage was envisaged to enhance both the selectivity and rate of O_2 reduction. Recently, mononuclear Fe-porphyrins having pendant residues like aliphatic amine, pyridine and guanidine etc. in the distal site, as envisaged above, (Scheme 1d) have demonstrated a 100 fold increase relative to previously reported heme and heme/Cu systems in the rate of oxygen reduction with >95% 4e$^-$/4H$^+$ selectivity even under slow electron fluxes from the electrode.[35] Kinetic and spectroscopic investigations in organic solutions indicated that the protonated amines can rapidly cleave the O−O bond heterolytically forming compound I with activation barriers of ∼12.5 kcal/mol only explaining the rate acceleration and high selectivity exhibited by these mononuclear iron porphyrins during oxygen reduction reaction (ORR) in aqueous medium. Thus, the reduction of Fe^{III}−OOH during electrochemical ORR in an aqueous medium likely involves a proton transfer step (PT) followed by electron transfer (ET) to the ensuing compound I species; that is, the reaction proceeds via PTET.[36] The active site of CcO, however, does not have such pendant bases; rather, it has the tyrosine residue with a phenol headgroup and can still exhibit a selective reduction of O_2 to H_2O. In a recent report on a heme/Cu system, a combination of kinetic experiments and theoretical calculations suggests that the conversion of end-on Fe^{III}-peroxo-Cu^{II} to Fe^{IV}-oxo-Cu^{II}−OH-PhȮ (intermediate analo-

Scheme 2. A General Mechanism of O_2 Reduction by Iron Porphyrins Indicating the Fate of the Key Fe^{III}−OOH Species As Observed using SERRS-RDE under Heterogeneous Aqueous Conditions

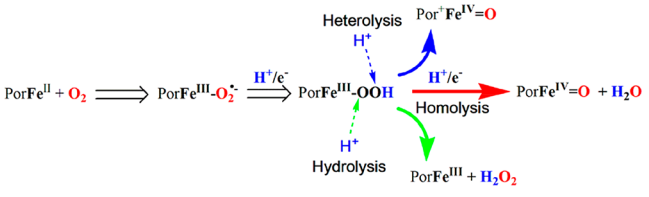

https://dx.doi.org/10.1021/jacs.0c10385
J. Am. Chem. Soc. XXXX, XXX, XXX−XXX

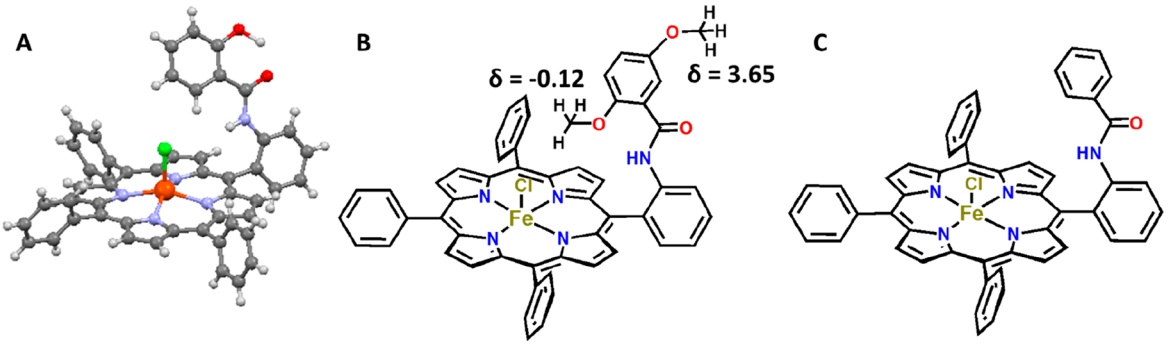

Figure 1. (A) X-ray structure of FePh, (B) schematic representation of $FeQMe_2$ indicating the -OMe ^1H resonances, (C) schematic representation of FeBz.

gous to P_M in CcO) proceeds through a transition state (TS), where a H-bonding interaction from PhOH cleaves the O−O bond homolytically prior to the proton coupled electron transfer (PCET) from the PhOH residue as indicated by experimental and theoretical values of the kinetic isotope effect (KIE) of the reaction.[18] Very recently, H-bond assisted O−O bond homolysis has been reported for a ferric hydroperoxide complex during the reduction of O_2 in an organic medium by a mononuclear Fe porphyrin having a hydroquinone ring covalently attached in the distal superstructure (Scheme 1e, $FeQH_2$).[37] The complex utilizes two consecutive hydrogen atom transfer (HAT) steps to reduce oxygen to water completely via ferric superoxide, ferric hydroperoxide, and ferryl oxo intermediate species. A similar HAT by heme superoxide complexes has recently been observed in other heme systems.[38−40] Thus, the crucial O−O bond cleavage of an intermediate ferric peroxide species is reported to be aided by PTET (heme/distal base, Scheme 1d), PCET (heme/Cu/Phenol, Scheme 1c), as well as HAT (heme/Quinol, Scheme 1e), albeit in very different systems.[37] Both phenol and hydroquinone are known to participate in PCET reactions in nature as well. Phenol is involved in oxygen reduction reaction by CcO in its mixed-valent form, while hydroquinone is found to donate a proton and electron to cytochrome C in Q-cytochrome c oxidoreductase, known as complex III, during electron transport in mitochondria.[18,41,42] Phenols and quinols are active participants in the reactivity of several Cu enzymes and related synthetic complexes.[43,44] However, it is still unknown if these two residues can directly participate in oxygen reduction reaction when they are attached with a mononuclear Fe porphyrin macrocycle. Apart from its obvious relation to the active site of CcO, how these residues tune the mechanism (PCET, HAT, etc.) of the reaction is of fundamental interest. Thus, a systematic investigation into the role of groups like phenol and quinol, which are capable of participating in proton and electron transfer using concerted or independent steps, in a closely related molecular framework, into the rates and selectivity of ORR (either in solution or under heterogeneous conditions) is desirable.

In this manuscript, O_2 reduction is investigated by three porphyrins having a pendant hydroquinone (Scheme 1e, $FeQH_2$), phenol (Scheme 1e, FePh), and 2,5-dimethoxy phenyl ring (Scheme 1e, $FeQMe_2$) covalently attached to the porphyrin ring (Figure 1) both in organic solution as well as under heterogeneous electrochemical aqueous conditions. Quinol and phenol pendant groups can act as both H-bond donor and acceptor and can serve as both a proton and electron donor in distinct as well as concerted pathways, while the methylated quinol can only act as a H-bond acceptor. An iron porphyrin with a pendant phenyl group and FeTPP act as the control samples. The electrochemical data show that, while all of these complexes can selectively reduce O_2 by $4e^-/4H^+$ with more than 95% selectivity and with similar rates, the solution characterization of the intermediates involved shows that the mechanism of the O_2 reduction varies from PCET, HAT, and ETPT depending on the chemical nature of the pendant group. The experimental data, along with density functional theory (DFT) calculations, suggest that, while a preorganization of the pendant group is key, intrinsic thermodynamic parameters of the pendant hydroxyl groups and a lowering of the inner-sphere reorganization ($\lambda_{\text{inner-sphere}}$) for the PCET from $Fe^{III}-O_2^{\cdot-}$ to $Fe^{III}-OOH$ species by hydrogen bonding from these groups play a decisive role in determining the reactivity and mechanism of action.

2. METHODS AND MATERIALS

All reagents and solvents are purchased from commercial sources. Sodium sulphide is purchased from Merck. 2,5-Dimethoxy benzoic acid, 2-hydroxy benzoic acid, $FeBr_2$, 2,4,6-collidine, KPF_6, and $CDCl_3$ are purchased from Sigma-Aldrich. $^{18}O_2$ is purchased from Sigma-Aldrich and Icon Isotopes. The sample preparations for resonance Raman (rR) and electron paramagnetic resonance (EPR) experiments and the handling of air-sensitive materials are performed under an inert atmosphere inside the glovebox. Room-temperature ^1H NMR spectra are collected on a Bruker DPX-500 spectrometer. The EPR spectra are recorded on a JEOL instrument using either an Oxford flow cryostat (4 K) or liquid N_2 finger dewar (77 K). Resonance Raman data are collected using 413.1 nm excitation from a Kr^+ ion source (Sabre, Coherent Inc.) and a Trivista 555 triple spectrophotometer (gratings used in the three stages are 900, 900, and 1800/2400 grooves/mm) fitted with an electronically cooled Pixis charge-coupled device (CCD) camera (Princeton Instruments). The first two stages of the spectrometer are used as a tunable bandpass. X-ray single-crystal data are collected at 100 K on a Bruker D8VENTURE Microfocus diffractometer equipped with PHOTON II Detector, with Mo Kα radiation (λ = 0.710 73 Å), controlled by the APEX3 (v2017.3-0) software package. Raw data are integrated and corrected for Lorentz and polarization effects using the Bruker APEX II95/APEX III program suite.

3. EXPERIMENTAL PROCEDURE

All the porphyrins were synthesized starting from *o*-aminophenyl-tris(phenyl)-porphyrin (monoamine, 1a), which, in turn, was synthesized by condensation of 1 equiv of *o*-nitrobenzaldehyde, 3 equiv of benzaldehyde, and 4 equiv of pyrrole followed by a reduction of the nitro group by adding $SnCl_2$ in dilute HCl followed by purification via a silica gel column.

https://dx.doi.org/10.1021/jacs.0c10385
J. Am. Chem. Soc. XXXX, XXX, XXX−XXX

3.1. FePh. One equivalent of 2-methoxy benzoic acid is dissolved in dry tetrahydrofuran (THF) solvent. It is then reacted with 4 equiv of oxalyl chloride added dropwise under refluxing condition and kept under Ar atmosphere overnight. Excess oxalyl chloride is evaporated to get the acid chloride (quantitative yield) as a yellowish oil. It is then treated with *o*-aminophenyl-tris(phenyl)-porphyrin dissolved in dry THF in the presence of 4 equiv of dry triethylamine and kept overnight at RT. The reaction mixture is then evaporated, dissolved in dichloromethane (DCM) solvent, and washed with water in a separatory funnel. The organic part is extracted, dried over anhydrous Na_2SO_4, and evaporated via a rotary evaporator. The solid crude product is then purified with column chromatography with silica gel (60−120 mesh) and an 80% DCM-hexane solvent mixture as the eluent. The final product is a violet powder. Yield: (>90%).

The resulting porphyrin is dissolved in dry DCM and allowed to react with 50 equiv of BBr_3 for 20 h at 0 °C. It is then neutralized with a saturated aqueous solution of sodium bicarbonate. The reaction mixture is then evaporated, dissolved in DCM, and washed with water in a separatory funnel. The organic part is extracted and then dried over anhydrous Na_2SO_4 and evaporated via a rotary evaporator. The crude reaction mixture is then purified using column chromatography with silica gel (60−120 mesh) and a 60% DCM-hexane mixture. The final product is a reddish-brown powder. Yield: (80%). ^{1}H NMR (400mHz, $CDCl_3$) δ ppm = 11.51 (s, 1H), 8.90 (m, 8H), 8.27 (m, 7H), 8.15 (m, 8H), 7.82 (m, 4H), 7.81(m,1H), 7.78 (m,1H), 7.61 (d, 1H), 7.26 (s,1H), 6.5 (d, 1H), −2.61 (s, 2H) (Figure S2). Electrospray ionization mass spectrometry (ESI-MS) (positive ion mode in acetonitrile (ACN)): m/z (%) = 749 (100) (Figure S1).

The porphyrin ligand is then metalated using $FeBr_2$ in dry THF in the presence of 2 equiv of 2,4,6-collidine under Ar atmosphere. The excess $FeBr_2$ is removed by working up the reaction mixture with dilute HCl, and the complex is extracted using DCM. The organic part is then dried over anhydrous Na_2SO_4 and evaporated using a rotary evaporator. The crude product is then purified using column chromatography with silica gel (60−120 mesh) and a 1% methanol-DCM solvent mixture as the eluent. The final product is a deep purple powder. Yield: (70−75%) ESI-MS (positive ion mode in ACN): m/z (%) = 804 (100) (Figure S3). It exhibits paramagnetic shifts of the meso-phenyl protons in its ^{1}H NMR consistent with a high-spin (HS) ferric porphyrin (Figure S4). The structure of the molecule is further confirmed using single-crystal X-ray diffraction (Figure 1A).

3.2. FeQMe$_2$. 2,5-Dimethoxy benzoic acid is dissolved in dry DCM, and 10 equiv of thionyl chloride is added dropwise under a refluxing condition and kept under an Ar atmosphere for 4 h. Excess thionyl chloride along with solvent are then evaporated to get the corresponding acid chloride as a yellow oil in quantitative yields. It is then treated with *o*-aminophenyl-tris(phenyl)-porphyrin dissolved in dry DCM and stirred for another 3−4 h at 45 °C under Ar atmosphere. The reaction mixture is then neutralized with a saturated aqueous solution of sodium bicarbonate and extracted with DCM and water; it was dried over anhydrous Na_2SO_4 and evaporated using a rotary evaporator and purified by column chromatography on silica gel (60−120 mesh), where the desired product was obtained using an 80% DCM-hexane solvent mixture as the eluent. A violet colored compound was isolated. Yield: (80−85%); ^{1}H NMR (400mHz, $CDCl_3$) δ ppm = 8.93 (m, 8H), 8.22 (m, 6H), 8.02 (m, 1H), 7.91 (m, 11H), 7.81 (m, 2H), 7.66 (d, 1H), 7.51(s,1H), 5.5 (d, 1H), 3.65 (s, 3H), 1.62 (s, 1H), −0.12 (s, 2H), −2.60 (s, 2H) (Figure S6). ESI-MS (positive ion mode in ACN): m/z (%) = 794 (100) (Figure S5).

The resulting porphyrin ligand is then metalated with $FeBr_2$ in THF in the presence of 2 equiv of 2,4,6-collidine under an Ar atmosphere. The excess $FeBr_2$ is then removed when the reaction mixture is washed with dilute HCl (1:4 concentration HCl/water). The organic part is extracted with DCM, separated, dried over anhydrous Na_2SO_4, and evaporated using a rotary evaporator. It is then purified using column chromatography on silica gel (60−120 mesh), and the desired product is obtained using a 1% DCM-methanol solvent mixture as eluent. A deep purple colored compound is isolated. Yield: (∼80%). ESI-MS (positive ion mode in ACN): m/z = 847 (Figure S7). It exhibits paramagnetic shifts of the meso-phenyl protons in its ^{1}H NMR consistent with a high-spin ferric porphyrin (Figure S8).

3.3. FeBz. Benzoic acid was dissolved in dry DCM. 10 equiv of thionyl chloride was added to it under refluxing conditions and stirred for 4 h under an Ar atmosphere. The excess thionyl chloride was evaporated, and a solution of *o*-aminophenyl-tris(phenyl)-porphyrin in dry DCM was added to it. The green reaction mixture was refluxed for 2−3 h under an Ar atmosphere (Scheme S1). The resulting reaction mixture was neutralized with triethylamine, whereby it changed color to purple, and washed with water and extracted with DCM. The organic phase was separated, dried over Na_2SO_4, evaporated, and purified by column chromatography using silica gel (60−120 mesh). The desired product was obtained by using an 80% DCM-hexane solvent mixture as the eluent. The violet colored compound was isolated when the solvent was evaporated. Yield: 80%; ^{1}H NMR (400 mHz, $CDCl_3$) δ ppm = 8.93 (m, 8H), 8.21 (m, 7H), 7.93 (m, 1H), 7.86 (m, 10H), 7.59 (m,1H), 6.86 (t, 1H), 6.56(m,4H), −2.60 (s, 2H) (Figure S9), ESI-MS (positive ion mode in ACN): m/z (%) = 734 (100) (Figure S10).

The resulting porphyrin ligand was then metalated with $FeBr_2$ in THF in the presence of 2 equiv of 2,4,6-collidine under an Ar atmosphere. The excess $FeBr_2$ was then removed by working up the reaction mixture with dilute HCl (1:4 concentration HCl/water) and DCM. The organic part was then separated, dried over anhydrous Na_2SO_4, and evaporated using a rotary evaporator. It was then purified by column chromatography on silica gel (60−120 mesh) and using a 1% DCM-methanol solvent mixture as the eluent. A deep purple colored compound was isolated. It exhibits paramagnetic shifts of the meso-phenyl protons in its ^{1}H NMR spectrum consistent with a high-spin ferric porphyrin (Figure S11). Yield: 80%. ESI-MS (positive ion mode in ACN): m/z (%) = 787 (100) (Figure S12).

3.4. FeQH$_2$. FeQH$_2$ is synthesized according to the previously reported procedure.[37]

3.5. Resonance Raman. An Fe-porphyrin is dissolved in dry and degassed THF so that the concentration of the solution is 1 mM in iron porphyrin. It is then reduced to its ferrous form by adding 0.5 equiv of Na_2S (20 mM stock solution in MeOH) under an Ar atmosphere. A 200 μL portion of the stock solution of the reduced porphyrin is then taken in a sample tube. The reduced sample tubes are then oxygenated at −80 °C and frozen in liquid N_2 at specified times. Resonance Raman data of these sample are collected at 77 K (liquid N_2 dewar) using a 413 nm laser source.

3.6. Electron Paramagnetic Resonance. The sample preparation for the EPR experiment is very similar to that for the resonance Raman experiments. The only difference is that, for collecting the EPR data, the sample solution is taken in an EPR tube instead of a Raman tube. The EPR data are recorded using an X-band EPR instrument at 4 K in the case of FePh and at 77 K in the case of FeQMe$_2$.

3.7. Electrochemical Experiments. *3.7.1. Cyclic Voltammetry.* The cyclic voltammograms (CV) are recorded using a CH instrument potentiostat model (710D). A very dilute solution (∼1 mM) of Fe-porphyrins dissolved in $CHCl_3$ is physiadsorbed on an edge-plane graphite (EPG) electrode. The loosely bound iron porphyrins are removed by sonicating the electrode in MeOH for 30 s. The resultant EPG bearing physiadsorbed complexes are cleaned with deionized water and used as the working electrode. A Pt wire is used as a counter electrode, and a Ag/AgCl (saturated KCl) standard electrode is used as the reference electrode. Phosphate buffer solutions (100 mM in phosphate) are used to maintain the pH of an electrolyte solution containing 100 mM KPF_6.

3.7.2. Rotating Disk Electrochemistry (RDE). The RDE measurements are performed using a CHI 710D bipotentiostat along with a Pine Instruments modulated speed rotor fitted with an E6 series change-disc tip. The complex is physiadsorbed on an edge plane graphite electrode as described above. The RDE experiment is performed by measuring linear sweep voltammetry (LSV) at a scan rate of 10−100 mV/s at different rotation rates using Ag/AgCl (saturated KCl) reference and Pt counter electrodes.

https://dx.doi.org/10.1021/jacs.0c10385
J. Am. Chem. Soc. XXXX, XXX, XXX−XXX

Scheme 3. Synthetic Scheme of Preparation of FePh (1c) and $FeQMe_2$ (2b)

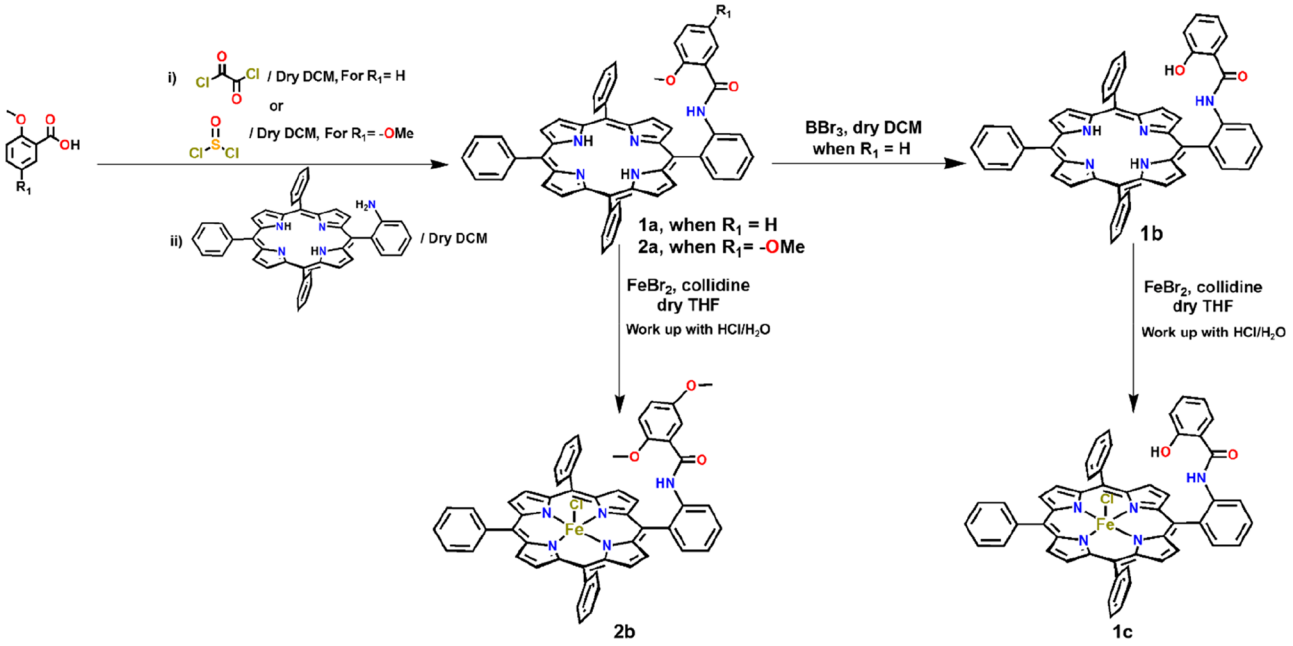

3.7.3. Rotation Ring Disk Electrochemistry (RRDE): Reactive Oxygen Species (ROS) Detection and Calculation. For RRDE experiments a Pt ring-disc assembly is used, where the Pt ring is placed encircling the disc electrode, and both Pt ring and the disc are used as working electrodes. The Pt ring is first cleaned by polishing it with alumina powder (grit sizes: 1, 0.3, and 0.05 μ) and then electrochemically using a cylindrical glass cell equipped with Ag/AgCl (saturated KCl) reference and Pt counter electrodes immersed into 0.5 M H_2SO_4 solution. In the RRDE technique, oxygen is reduced catalytically on the disk, whose potential is swept from positive to negative, and the Pt ring is held at a constant potential (0.7 V at pH7), where the partially reduced oxygen species such as superoxide peroxide, etc., produced during oxygen reduction on the disc gets oxidized resulting in an oxidation current. The PROS is the ratio of the $2e^-/2H^+$ ring current (corrected for collection efficiency) and the catalytic disc current and is normalized to 100%. The collection efficiency (CE) is evaluated at a 10 mV/s scan rate using 2 mM $K_3Fe(CN)_6$ and 0.1 M KNO_3 solutions at a rotation speed of 300 rpm. The CE is measured as 18 ± 1% during these experiments.

The RRDE was performed on the Fe porphyrins, which were physiadsorbed on edge plane graphite electrode as well as alkane thiol (C8-SH and C16-SH) self-assembled monolayers (SAM) modified gold electrode. The thiols are adsorbed on a freshly cleaned gold electrode by dipping freshly cleaned Au electrodes (disc or wafers) in a 0.1 mM ethanolic solution of the desired thiol solutions for 24 h to form uniform SAM. Dilute solutions of iron porphyrins in $CHCl_3$ are deposited on these SAM following the protocol used for the EPG electrodes.

3.8. Computational Details. DFT calculations are performed using the Gaussian 03 software package. Geometry optimizations are done with the B3LYP functional within an unrestricted formalism.[45,46] A mixed basis set consisting of 6-311G* on Fe and 6-31G* on other atoms is used for geometry optimization and frequency calculation.[47] The structures of the ferric superoxide complexes have been optimized using a broken symmetry approach.[48−51] All the optimized structures yielded no imaginary frequency. Tight self-consistent field (SCF) convergence and a 6-311+G* basis set in a polarizable continuum model were used on all atoms for single-point energy calculations. For the calculation of the reduction potential water is used as the solvent.

4. RESULTS

4.1. Synthesis. The porphyrin ligand with a pendant phenol is obtained via a multistep synthesis by first converting 2-methoxy benzoic acid to the corresponding acid chloride (Scheme 3). It is then refluxed with *o*-aminophenyl-tris-(phenyl)-porphyrin in dry DCM for 4−5 h to yield the corresponding amide (1a). Similarly, for the synthesis of the dimethylquinone substituent, 2,5-dimethoxy benzoic acid is converted to its acid chloride, which is then refluxed with *o*-aminophenyl-tris(phenyl)-porphyrin in the presence of dry DCM to obtain the corresponding amide (2a). The methoxy group in the distal phenyl ring of 1a is then demethylated to yield the corresponding phenol by treating the porphyrin with BBr_3 at 0 °C to result in ligand 1b. The ligands 1b and 2a are metalated with Fe using standard protocols to yield FePh and $FeOMe_2$ (Scheme 3). These porphyrins and iron complexes are characterized using ESI-MS and ^{1}H NMR. The FePh complex is further characterized using single-crystal X-ray diffraction, where the single crystals are obtained by a slow diffusion of acetonitrile into a chloroform solution of FePh (Figure 1A). The structure shows that the phenyl ring is atop the porphyrin ring. The chloride counterion is derived during purification, which involved a workup in dilute HCl. While the $FeQMe_2$ complex could not be crystallized, the ^{1}H NMR spectrum of the precursor complex 2a shows one of the two −OMe singlets at −0.12 ppm. Such an upfield shift of the −OMe group (3.65 ppm) is due to the aromatic current of the porphyrin ring implying that the −OMe group is oriented above the porphyrin plane (Figure 1B). The control FeBz complex, which does not possess any of the pendant groups, is synthesized by the condensation of *o*-aminophenyl-tris-(phenyl)-porphyrin with benzoyl chloride followed by subsequent metalation of the porphyrin with $FeBr_2$.

4.2. Heterogeneous Electrochemistry. The complexes FePh, $FeQMe_2$, and $FeQH_2$ are adsorbed on an EPG electrode, and their CV data, in degassed pH 7 buffer solution, show the $Fe^{III/II}$ E^0 (Figure 2A−C) at −310, −170, and −250 mV versus Ag/AgCl (saturated KCl) reference, respectively. In addition

https://dx.doi.org/10.1021/jacs.0c10385
J. Am. Chem. Soc. XXXX, XXX, XXX−XXX

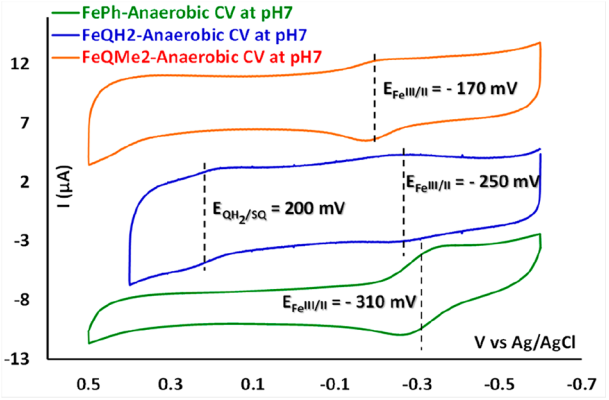

Figure 2. Anaerobic CV of $FeQMe_2$ (orange), $FeQH_2$ (blue), and FePh (green) physiadsorbed on an EPG electrode immersed in pH 7 buffer solution in the presence of Ag/AgCl (saturated KCl) reference electrode and Pt counter electrode. The data were recorded at a scan rate 500 mV/s at 25 °C.

to the $Fe^{III/II}$ process at −250 mV, the quinol (QH_2) to semiquinone (SQ) CV is observed at +200 mV versus Ag/AgCl (saturated KCl) for the $FeQH_2$ complex (Figure 2b). The plot of both the $Fe^{III/II}$ and SQ/QH_2 E^0 versus pH (Figure 3A, simulation to the data points—brown and red lines) shows a slope of 60 mV/pH suggesting that both these processes involve $1e^-/1H^+$ PCET. Similarly, the $Fe^{III/II}$ process for the FePh is also a $1e^-/1H^+$ PCET as indicated by the slope (60 mV/pH) of E^0 versus pH in the plot (Figure 3B, simulation to data points—red line) of FePh. In all these cases the Br^- counterion bound to the resting ferric complex synthesized is exchanged with OH^- in the aqueous medium. The reduction of this Fe^{III}—OH center is associated with the protonation of the hydroxide ligand to water resulting in the PCET behavior of the $Fe^{III/II}$ process, that is, Fe^{III}—OH + e^- + H^+ → Fe^{II}—OH_2.

4.2.1. Electrocatalytic Oxygen Reduction. The electrode bearing these complexes is immersed in an air-saturated pH 7 buffer, and on sweeping the potential below the E^0 of $Fe^{III/II}$, the CV is replaced by an electrocatalytic oxygen reduction current. Electrochemical ORR is characterized by rate, onset potential, and selectivity ($2e^-/2H^+$ vs $4e^-/4H^+$). The rate and selectivity of the ORR by these iron porphyrins catalyzing ORR on EPG electrodes can be assessed by a Koutechy-Levich (K-L) analysis of RDE data.[52] In this experiment, the linear sweep voltammetry data of oxygen reduction by an Fe-porphyrin complex, physiadsorbed on an edge plane graphite electrode, are collected at different rates of rotation. The catalytic current of oxygen reduction increases with an increase in rotation rate following eqs i and (ii). The number of electroactive species on the electrode is estimated by performing CV in the absence of O_2 before conducting the ORR experiments. The inverse of current in a mass-transfer limited region varies linearly with the inverse of the square root of the angular rate of rotation, and the plot yields both the second-order rate constant of ORR (eq i, calculated from the intercept of the K-L plot) as well as the number of electrons provided to the substrate, O_2 (n in eq ii, calculated from the slope of the K-L plot). The plot of $\omega^{-1/2}$ with I^{-1} at −0.4 V potential for FePh (Figure 4A), $FeQH_2$ (Figure 4C), and $FeQMe_2$ (Figure 4E) yields second-order rate constants of $(7.09 \pm 1) \times 10^6$ M^{-1} s^{-1}, $(1.97 \pm 1) \times 10^6$ M^{-1} s^{-1}, and $5.31 \pm 2) \times 10^7$ M^{-1} s^{-1}, respectively, and the slope (inset) of all of these complexes indicates that they reduce oxygen by $4e^-/4H^+$ to H_2O. Thus, these mononuclear iron porphyrins reduce O_2 to H_2O at very similar rates in pH 7 buffer solution when adsorbed on graphite electrodes. Alternatively, the control FeBz complex decays during oxygen reduction such that reproducible K-L analysis could not be achieved. Such a decay is generally associated with the generation of PROS, that is, lower selectivity for $4e^-/4H^+$ reduction. The selectivity for ORR, however, is much more accurately determined using rotating ring disc electrochemistry (RRDE) and is described below.

$$I^{-1} = i_k^{-1} + i_l^{-1} \quad \text{(i)}$$

$$i_l = 0.62nFA[O_2](D_{O2})^{2/3}\omega^{1/2}\nu^{-1/6} \quad \text{(ii)}$$

At pH 7, the onset potential of the ORR currents obtained using the FePh and $FeQH_2$ complexes align with the $Fe^{III/II}$ E^0 (Figure 4B,D), indicating that the reduction of the Fe^{III} to Fe^{II} is the most thermodynamically uphill process in the ORR catalytic cycle. However, the onset potential of the ORR current for the $FeQMe_2$ complex is cathodically shifted by 130 mV with respect to the $Fe^{III/II}$ process, indicating that the ORR involves at least one step that requires more driving force than

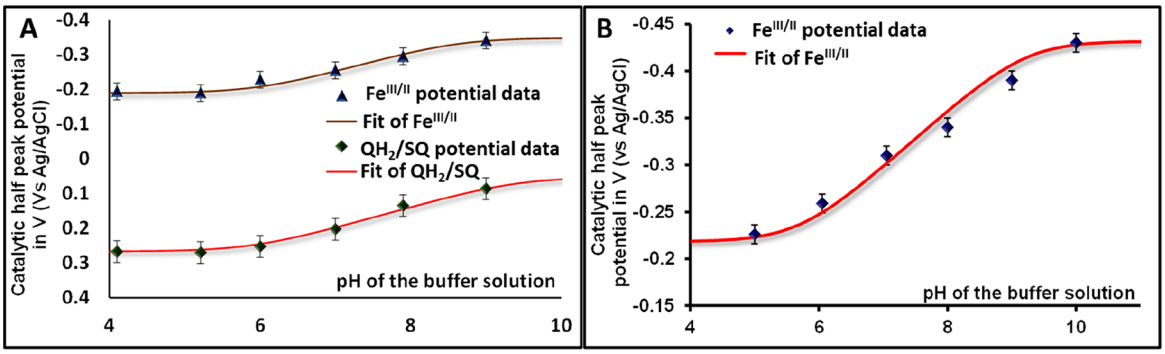

Figure 3. (A) CV data of $FeQH_2$ physiadsorbed on EPG are collected in a buffer solution having different pH. Plot of the potential of the Fe^{III}/Fe^{II} redox couple and a semiquinone/hydroquinone redox couple vs pH of the deoxygenated buffer solution (blue triangles and green diamonds, respectively) and the simulation of the pH dependence using a PCET formalism (brown and red lines, respectively). (B) CV data of FePh physiadsorbed on EPG are collected in buffer solutions having different pH values. Plot of the potential of the Fe^{III}/Fe^{II} redox couple vs pH of the deoxygenated buffer solution shows a 60 mV shift of the $Fe^{III}/^{II}$ redox potential per unit change in pH (blue diamonds) and the simulation of the pH dependence using a PCET formalism (red line).

https://dx.doi.org/10.1021/jacs.0c10385
J. Am. Chem. Soc. XXXX, XXX, XXX−XXX

$$I^{-1} = i_k^{-1} + i_l^{-1} \text{ ----------(i)}$$

$$i_l = 0.62nFA[O_2](D_{O_2})^{2/3}\omega^{1/2}\nu^{-1/6} \text{ ----(ii)}$$

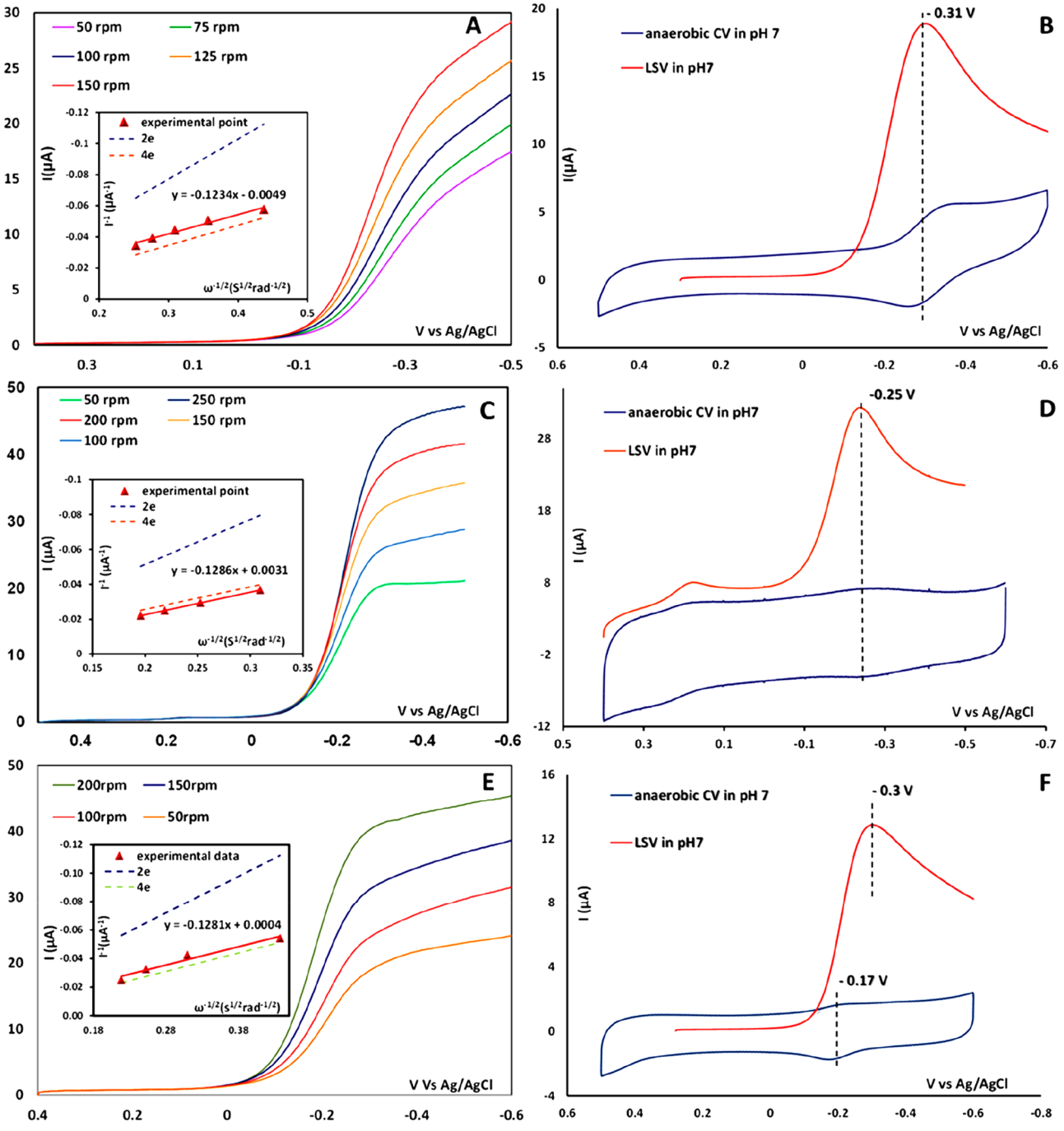

Figure 4. RDE and LSV data of FePh (A, B), $FeQH_2$ (C, D), and $FeQMe_2$ (E, F) deposited on an EPG surface in pH 7 phosphate buffer using 100 mM KPF_6 as the supporting electrolyte and Ag/AgCl (saturated KCl) and Pt as reference and counter electrodes, respectively. The RDE data were collected at multiple rotations. (inset) K-L plot of Fe porphyrins is represented by a solid line. The theoretical plots for $4e^-$ and $2e^-$ processes are indicated by dashed lines in red and blue, respectively. LSV and RDE data were recorded at 100 mV/s scan rate, while the CV were recorded at 500 mV/s.

the reduction of Fe^{III} to Fe^{II} (Figure 4F). Note that, in the presence of oxygen, the $Fe^{III/II}$ reduction wave was not observed in $FeQMe_2$, as O_2 binding to ferrous iron porphyrins (EC step) are of the order of 10^3 s^{-1} (the second-order rate constant is $\sim 10^7$ $mol^{-1}s^{-1}$, and the oxygen concentration is 0.2 mM in water[8]), and the resulting 1e prewave is buried under the large catalytic wave, as the latter is almost 2 orders of magnitude higher than the former. Indeed, the reduction potential of $Fe^{III}-O_2^-$ is measured to be lower relative to Fe^{III} in organic solvents in the absence of protons.[53] The pH dependence of ORR (defined as the peak potential of the electrocatalytic ORR current) of $FeQH_2$ and $FeQMe_2$ show

https://dx.doi.org/10.1021/jacs.0c10385
J. Am. Chem. Soc. XXXX, XXX, XXX−XXX

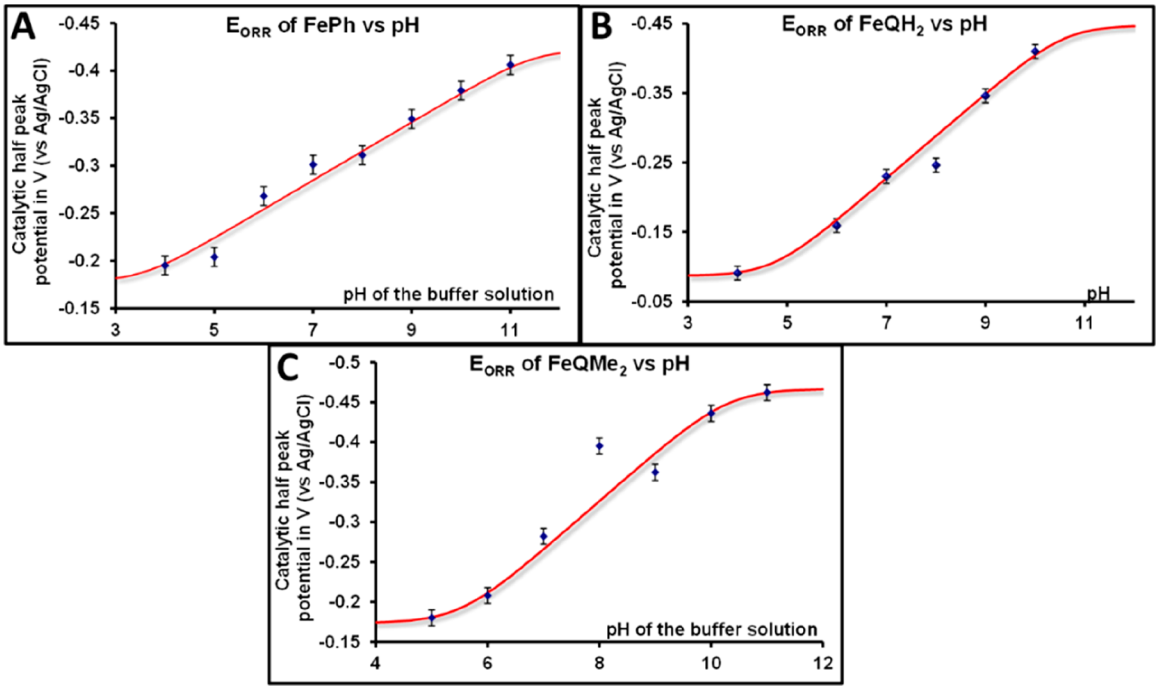

Figure 5. Plot of E_{ORR} vs pH for (A) FePh, (B) $FeQH_2$, and (C) $FeQMe_2$ molecules physiadsorbed on EPG immersed in buffer solutions having different pH (data are in blue diamonds, and the corresponding PCET simulation is shown in the red line). The data were recorded in the presence of a Ag/AgCl reference electrode and Pt counter electrode at 25 °C. All the cyclic voltammograms were recorded at a 500 mV/s scan rate.

the same $1e^-/1H^+$ slope similar to the pH dependence of the $Fe^{III/II}$ process for these complexes (Figure 5B,C). The pH dependence of the E_{ORR} of the FePh complex (Figure 5A) has a slope of 30 mV/pH, indicative of a $2e^-/1H^+$ PCET step as the potential defining step of the ORR. This is different from that of the pH dependence of the E^0, which is $1e^-/1H^+$ PCET. The $2e^-/1H^+$ dependence can be due to a second ET step having a higher or the same E^0 as the $Fe^{III/II}$ involved in the ORR catalysis.[54] The differences in onset potential and pH dependencies clearly suggest that, despite similarities in the catalytic ORR rates, the mechanism of the ORR is different for these different porphyrins, which vary only marginally in their distal substituents.

4.2.2. Measurement of Amount of Partially Reduced Oxygen Species during Reduction of Oxygen. A $4e^-/4H^+$ ORR by mononuclear iron porphyrins with selectivity as high as 95% is very rare. Most mononuclear iron porphyrins show a substantial (30−100%) $2e^-/2H^+$ ORR forming H_2O_2.[25−28] In situ resonance Raman spectroscopy has revealed that the fate of an Fe^{III}−OOH intermediate, which accumulates under a steady state and is detected using resonance Raman, formed during ORR is mostly responsible for the generation of H_2O_2 (Scheme 4).[29,55] Depending on the axial ligand on the iron porphyrin, this intermediate species is either protonated or reduced for O−O bond cleavage (i.e., the next step of $4e^-/4H^+$ ORR).[34] However, if protons and electrons are not provided rapidly, the Fe^{III}−OOH hydrolyzes to produce H_2O_2, that is, $2e^-/2H^+$ ORR. In iron porphyrin complexes with pendant amines that are protonated at neutral pH values and deliver protons to the unbound distal oxygen atom of the Fe^{III}−OOH species, the O−O bond heterolysis is very facile, which rescinds the possibility of PROS production via a hydrolysis of the Fe^{III}−OOH intermediate.[35] The heterolysis of the O−O bond of a ferric peroxide of these porphyrins to result in compound I has recently been established in organic solutions

Scheme 4. Schematic Representation of a General Mechanism of Oxygen Reduction by Synthetic Fe Porphyrins

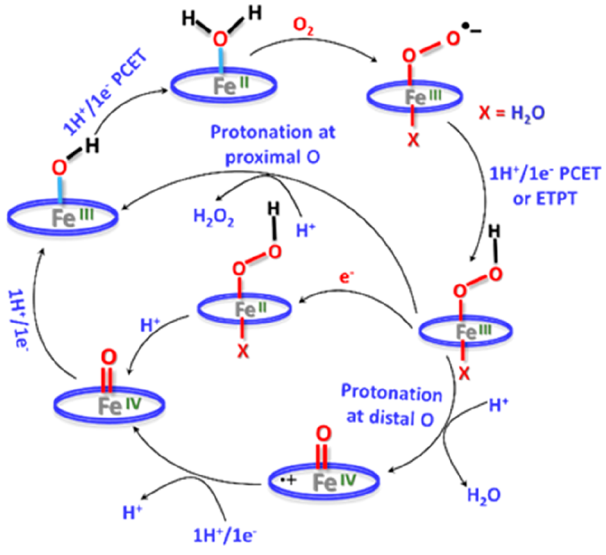

using rapid kinetics, EPR, and reactivity.[36] Hydrolysis of the Fe^{III}−OOH intermediate formed during ORR is accentuated by slowing down electron transfer (ET) from the electrode to the catalyst, which enhances the extent of competitive hydrolysis of this intermediate. Slowing down of the ET from the electrode can be achieved by immobilizing these catalysts on SAM of thiols on Au electrodes, where the rate of ET across these electrodes can be attenuated between 10^5 and 10 s^{-1} by extending the chain length of the thiol.[19,56] These complexes are immobilized on octanethiol SAM (C_8SAM) and hexadecanethiol (C_{16}SAM), where the rates of ET are $\sim 10^3$ and ~ 10 s^{-1}, respectively, and the extent of H_2O_2 released is

https://dx.doi.org/10.1021/jacs.0c10385
J. Am. Chem. Soc. XXXX, XXX, XXX−XXX

assessed using RRDE. In RRDE any H_2O_2 released on the working electrode is diffused to and can be reoxidized at a Pt ring electrode, encircling the working Au disc electrode by poising a constant potential on it, while the ORR current is investigated at the working electrode.[52] Thus, an assessment of the extent of H_2O_2 released under very slow ET fluxes allows a direct investigation of the inherent reactivity of the Fe^{III}−OOH intermediate; that is, larger PROS reflect a lower stabilization and/or slower rate of O−O bond cleavage. The data (Table 1, Figure S13 blue) show that FePh, $FeQH_2$, and $FeQMe_2$ produce only 4.0 ± 0.5, 3.3 ± 0.2, and 1.8 ± 0.5% PROS on EPG electrodes, respectively. The data on the EPG electrode are consistent with the RDE data, which showed a selective $4e^-/4H^+$ ORR for all of these complexes as well. The FePh as well as the $FeQH_2$ complexes show a very selective $4e^-/4H^+$ ORR even under very slow ET rates, with a maximum of 4% PROS (Table 1, rows 1 and 2, Figure S13), suggesting that either these complexes have an inherent mechanism for promoting the O−O bond cleavage or these complexes can stabilize the Fe^{III}−OOH intermediate, substantially avoiding their hydrolysis. In contrast, the $FeQMe_2$ complex shows a gradual increase in the PROS from 1.8% to 10% (i.e., a fivefold increase, Table 1 row 3, Figure S13) as the ET rate is slowed. The behavior of $FeQMe_2$ is similar to iron porphyrins without distal architectures, where as much as 100% PROS has been reported on C_{16}SAM, albeit the effect of slow ET is quite demure in $FeQMe_2$ relative to the iron porphyrins reported previously (Table 1, rows 5 and 6) for reasons discussed later. RRDE data on control samples FeBz (Figure 1C) and previously reported FeTPP show higher PROS during electrochemical ORR (Figure S15, Table 1). Thus, the three synthetic model complexes ($FeQH_2$, FePh, and $FeQMe_2$) used herein impress on the profound role of distal residues on enhancing the selectivity of ORR by mononuclear iron porphyrins despite having potentially very different mechanisms for achieving the same.

Table 1. % of PROS Produced by Fe Porphyrins on Different Electrodes

complex	EPG (k_{ET} = $10^6 s^{-1}$)	C_8SAM modified Au (k_{ET} = $10^3 s^{-1}$)	C_{16}SAM modified Au (k_{ET} = 6−10 s^{-1})	refs
$FeQH_2$	3.3 ± 0.2	5.5 ± 0.6	3.3 ± 0.4	this work (Figure S14A)
FePh	4.0 ± 0.5	3.2 ± 0.3	3.6 ± 0.4	this work (Figure S14B)
$FeQMe_2$	1.8 ± 0.5	4.6 ± 0.2	10.2 ± 0.5	this work (Figure S14C)
FeBz	11 ± 0.5	18 ± 1	27 ± 2	this work (Figure S15)
FeTPP	10	29	rapid degradation	35

Despite similar rates, the onset potential and its pH dependence and selectivity under different ET rates of ORR by these three complexes in buffered aqueous solutions indicate that very different ORR mechanisms are at play for these complexes. In the FePh complex, where there is a pendant phenol, the ORR rate constant is (7.09 ± 1) × 10^6 M^{-1} s^{-1}, a $2e^-/1H^+$ PCET onset potential that overlays with that of $Fe^{III/II}$ E^0 at pH 7, and the selectivity of ORR stays at $4e^-/4H^+$ even under a slow ET flux. The $FeQH_2$ complex, with a quinol, shows an ORR rate constant of (1.97 ± 1) × 10^6 M^{-1} s^{-1}, a $1e^-/1H^+$ PCET onset potential that overlays with the $Fe^{III/II}$ E^0 at pH 7, and the selectivity stays at $4e^-/4H^+$ even under a slow ET flux. The $FeQMe_2$ complex, where the hydroxyl groups of $FeQH_2$ are methylated, show an ORR rate of (5.31 ± 2) × 10^7 M^{-1} s^{-1} on EPG, an $1e^-/1H^+$ PCET onset potential that is shifted cathodically relative to the $Fe^{III/II}$ E^0 at pH 7, and the selectivity for the $4e^-/4H^+$ ORR is gradually reduced at slow ET fluxes. To gain insight into these differences, the reaction of the reduced ferrous FePh, $FeQH_2$, and $FeQMe_2$ with O_2 is monitored in an organic medium.

4.3. Reaction with O_2 in Organic Solution. The FePh, $FeQH_2$, and $FeQMe_2$ complexes are reduced to their ferrous forms, and their reaction with O_2 is followed at −80 °C (dry ice/MeOH bath) to trap and characterize the reaction intermediates and elucidate the mechanism of O_2 activation by these complexes. The reduced $FeQMe_2$ complex when exposed to dry O_2 gas forms an EPR-silent species. The resonance Raman data of this species exhibit the oxidation and spin-state marker bands ν_4 and ν_2 at 1368 and 1568 cm^{-1}, respectively, consistent with the formation of a low-spin (LS) Fe(III) species in solution (Figure S16A). The Fe−O vibration of this diamagnetic Fe^{III}−$O_2^{\cdot-}$ species is observed at 585 cm^{-1} and is confirmed by a 28 cm^{-1} shift to 557 cm^{-1} on using ^{18}O-labeled O_2 gas (Figure 6).[57] This Fe^{III}−$O_2^{\cdot-}$ species does not react any further and, with time, hydrolyzes to regenerate the ferric porphyrin (Scheme 5C). Note that the $FeQMe_2$ complex needs an additional thermodynamic driving force for catalyzing an ORR under heterogeneous conditions in an aqueous solvent, indicting that the oxy adduct produced in either aqueous or nonaqueous medium is not capable of taking the reaction forward toward ORR. The reaction of the reduced $FeQH_2$ complex has been recently reported in detail.[37] The $FeQH_2$ complex forms a Fe^{III}−$O_2^{\cdot-}$ species that performs an HAT from the pendant quinol generating a [Fe^{III}−OOH]SQ species (Scheme 5A). This species is characterized by the EPR and rR of the Fe^{III}−OOH unit with the help of ^{18}O and ^2H substitution. The [Fe^{III}−OOH]SQ species then undergoes another HAT to form a [Fe^{IV}═O]Q species, which is characterized by an Fe−O vibration at 750 cm^{-1} and the symmetric quinone mode at 1520 cm^{-1}. The kinetics of formation and decay of these intermediates are investigated

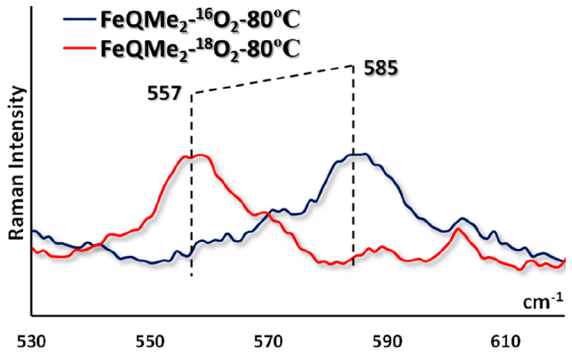

Figure 6. Resonance Raman data of the superoxide complex of $FeQMe_2$. The blue spectra represent the $^{16}O_2$ adduct of $FeQMe_2$, and the red one represents the $^{18}O_2$ adduct of $FeQMe_2$.

https://dx.doi.org/10.1021/jacs.0c10385
J. Am. Chem. Soc. XXXX, XXX, XXX−XXX

Scheme 5[a]

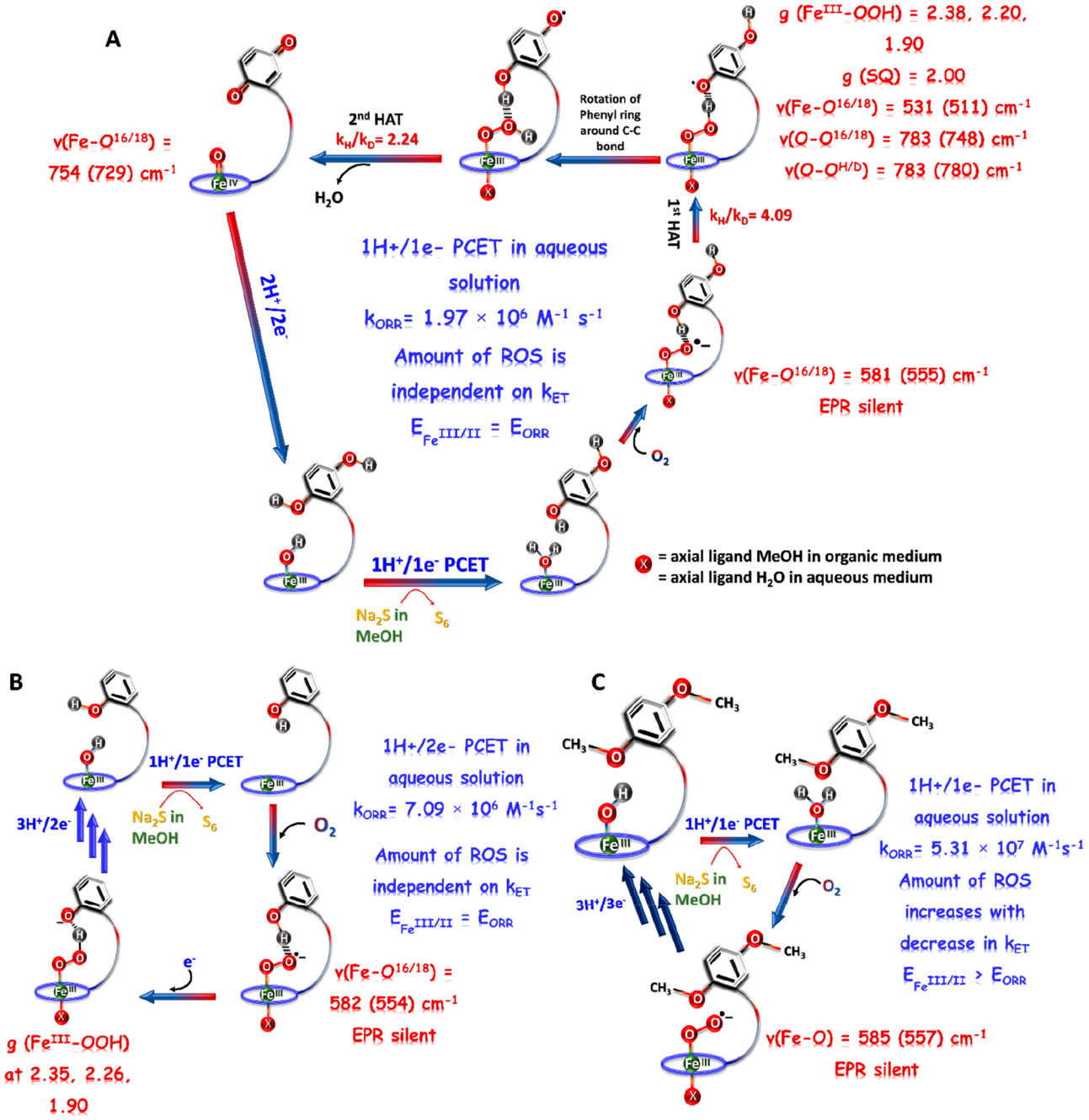

[a](A) Schematic representation of a mechanism of an ORR by $FeQH_2$ involving a double HAT pathway. (B) Schematic representation of a mechanism of an ORR by FePh involving a disproportionation reaction of ferric superoxide complex. (C) Schematic representation of an ORR by $FeQMe_2$ in organic and aqueous mediums. The red and blue colors are used to denote features observed in organic and aqueous mediums, respectively. The features colored with both red and blue are proposed to occur in both the mediums.

using EPR, and ^2H isotope effects are consistent with two consecutive HATs (Scheme 5A). Thus, once reduced, the $Fe^{III}-O_2\cdot^-$ species formed upon oxygen binding can complete ORR without any additional electron from an external source, which is consistent with the fact that ORR proceeds at the $Fe^{III/II}$ potential under heterogeneous conditions in aqueous solvents.

The reduced FePh complex reacts with O_2 gas to form an $Fe^{III}-O_2{:}^-$ species characterized by a diamagnetic ground state with no EPR signal. The rR data of this species show the oxidation-state marker band ν_4 at 1369 cm^{-1} and the spin-state marker band ν_2 1568 cm^{-1} characteristic of low-spin Fe^{III} ground state (Figures 7B and S16). The Fe−O vibration of this $Fe^{III}-O_2{:}^-$ species is at 582 cm^{-1}, which shifts to 554 cm^{-1} on $^{18}O_2$ substitution (Figure 7A). Note that the Fe−O stretching frequency is lower than that of $FeQMe_2$ and similar to that of the previously characterized ferric superoxide intermediate of $FeQH_2$ and other Fe-porphyrins having H-bonded triazole residues in the distal pocket.[37,57,62] A H-bonding interaction between the hydrogen-bond donor and $Fe^{III}-O_2{:}^-$ leads to a reduction in the Fe−O stretching frequency.[62] The $Fe^{III}-O_2\cdot^-$ species evolves into a mixture of high-spin and low-spin species

https://dx.doi.org/10.1021/jacs.0c10385
J. Am. Chem. Soc. XXXX, XXX, XXX−XXX

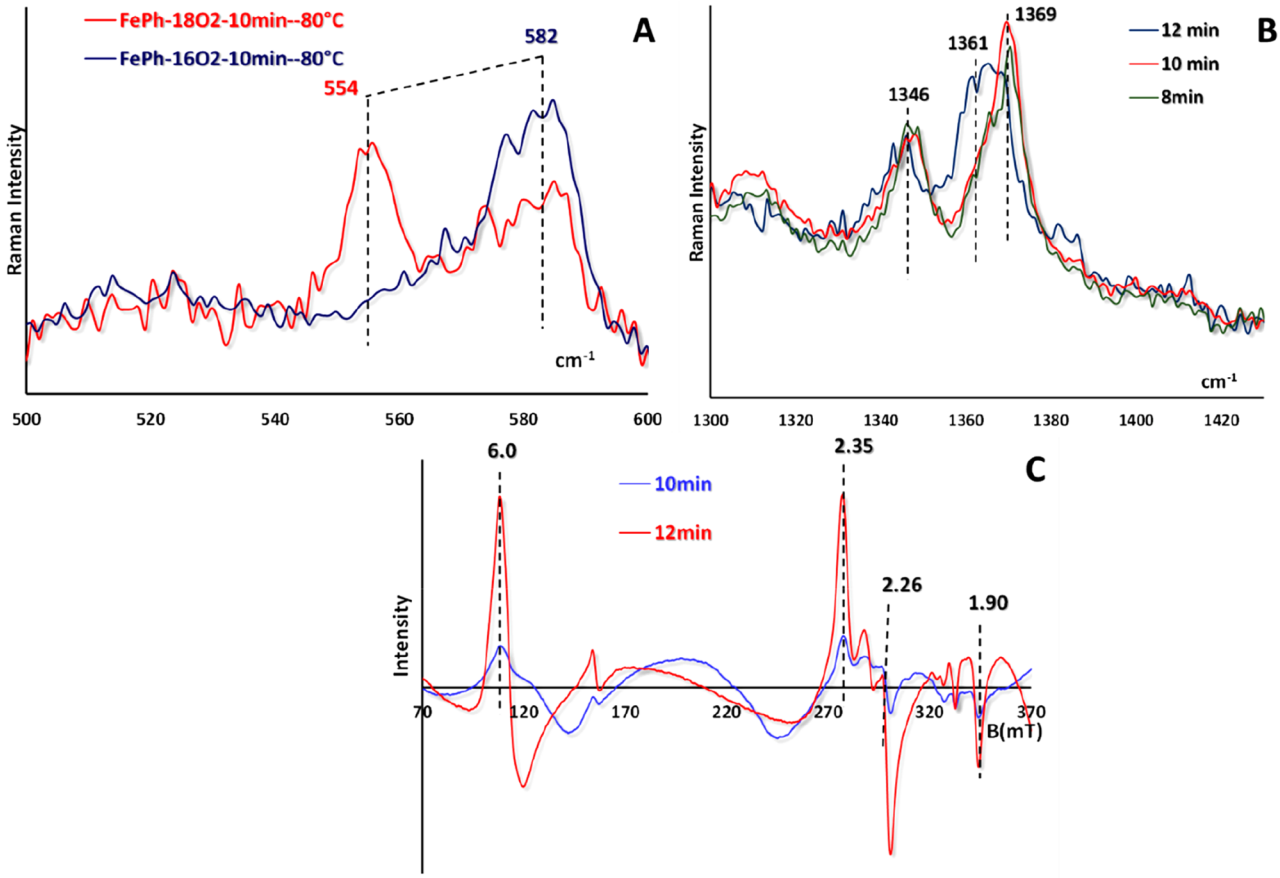

Figure 7. (A) Resonance Raman data of a superoxide complex of FePh. The blue spectrum represents the $^{16}O_2$ adduct of FePh, and the red one represents the $^{18}O_2$ adduct of FePh. (B) Oxidation-state marker (ν_4) of ferric superoxide and ferric hydroperoxide species of FePh. When the reduced FePh is oxygenated at −80 °C and allowed to react with O_2 for 8 min it shows a maximum Fe^{III} low-spin signal (ν_4 at 1367 cm^{-1}) corresponding to a ferric superoxide complex (green spectra). When the sample is kept at −80 °C for 10 min ferric superoxide begins to form ferric hydroperoxide (red spectra), and after 12 min some amount of low-spin signal (corresponding to ferric superoxide) significantly decreases, and the oxidation-state marker (1361 cm^{-1}) for the high-spin ferric complex increases (blue spectra), which confirms the disproportionation reaction of ferric superoxide to ferric hydroperoxide and HS ferric complex. (C) EPR data of ferric hydroperoxide complex of FePh recorded at 4 K. The intensity of the EPR signal of both Fe^{III} HS and Fe^{III} LS species increases simultaneously with time. The blue spectrum represents the EPR signal of a ferric hydroperoxide complex incubated at −80 °C for 10 min, and the red spectrum represents the EPR signal of the same intermediate species with an incubation period of 12 min in a −80 °C bath.

with the ν_4 and ν_2 values at 1361 and 1555 cm^{-1} and 1369 and 1568 cm^{-1}, respectively. Consistently, the corresponding EPR spectra shows the presence of a signal at $g = 6$ corresponding to the high-spin ferric species and a low-spin ferric species with g-values at 2.35, 2.26, and 1.90 (Figure 7C). These g-values are consistent with those of 6C low-spin ferric hydroperoxide (Fe^{III}−OOH) complexes (Table 2) reported in the past.

Table 2. g Values of Previously Reported Ferric Heme Hydroperoxide Complexes

name of ferric heme hydroperoxide complex	g values	ref
(TMPIm)Fe^{III}−OOH	2.32, 2.19, 1.95	58
(TMPIm)Fe^{III}−OOH	2.31, 2.19, 1.95	59
Fe^{III}−F_{20}TPP−OOH	2.26, 2.14, 1.96	53
HOO-met-hemoCD−OH	2.26, 2.16, 1.96	60
HOO-met-hemoCD-Im	2.32, 2.19, 1.94	60
Fe^{III}-TPP−OH-OOH	2.27, 2.16, 1.96	61
Fe^{III}OEP−OH-OOH	2.29, 2.17, 1.95	61
$FeQH_2$-MeOH-OOH	2.38, 2.20, 1.90	37
FePh-MeOH-OOH	2.35, 2.26, 1.90	this work

Similar g-values are also obtained for the same intermediate of $FeQH_2$ in a previous report using the $FeQH_2$ complex, which are confirmed by an $^{16}O_2/^{18}O_2$ and H/D isotope shift of Fe−O and O−O vibrations in its resonance Raman spectra.[37] While for the ferric hydroperoxide intermediate of FePh the Fe−O and O−O vibrations could not be identified in the rR data, the ν_4 and the ν_2 values are at 1369 and 1568 cm^{-1} (Figures 7B and S16), respectively, consistent with those of low-spin iron porphyrin as observed in the EPR data. These observations here are very similar to those reported for iron porphyrins bearing pendant −COOH groups, where an Fe^{III}−$O_2^{\bullet-}$ adduct is reduced to an Fe^{III}−OOH via an intramolecular $1e^-/1H^+$ PCET process, where the proton is delivered from the pendant −COOH group and the electron is derived from unreacted Fe^{II} species in solution.[63] Considering the data obtained here and previous literature precedence, the FePh reacts with O_2 to form a Fe^{III}−$O_2^{\bullet-}$ species initially, which is then transformed to an Fe^{III}−OOH species via an intramolecular PCET, where the proton is delivered from the pendant phenol and the electron is derived from another Fe^{III}−$O_2^{\bullet-}$ complex present in solution (Scheme 5B). The Fe^{III} high-spin species thus generated by an oxidation of the Fe^{III}−$O_2^{\bullet-}$ species results in

https://dx.doi.org/10.1021/jacs.0c10385
J. Am. Chem. Soc. XXXX, XXX, XXX−XXX

an increase in the $g = 6$ signal (Figure 7C) in the EPR and new ν_4 and ν_2 vibrations at 1361 and 1555 cm^{-1}, respectively. The rise of these high-spin ferric ν_4 and ν_2 is associated with the concomitant decrease of the ν_4 (Figure 7B) and ν_2 (Figure S17) vibrations at 1369 and 1567 cm^{-1} originating from the $Fe^{III}-O_2^{\cdot -}$ species. Curiously, the electron required to reduce the $Fe^{III}-O_2^{\cdot -}$ is derived from another $Fe^{III}-O_2^{\cdot -}$ species. Thus, one may expect that the ORR should occur at the same potential where Fe^{III} is reduced to Fe^{II}, which is exactly what happens under heterogeneous aqueous conditions. Eventually, this intermediate decays to form a single high-spin species with ν_4 and ν_2 vibrations at 1361 and 1555 cm^{-1}, respectively (Figure S16B).

4.4. Reconciliation of the Reactivities in Aqueous and Organic Solvents. The $FeQMe_2$ complex with the methylated quinol can bind O_2 in an organic solution in its ferrous state but cannot take the reaction forward. This is consistent with the onset potential of an ORR in an aqueous medium being lower than the E^0 $Fe^{III/II}$. The $Fe^{III}-O_2^{\cdot -}$ species immediately formed upon reduction of the iron to its ferrous form is incapable of reacting further, unless an additional electron is provided from the electrode at a higher thermodynamic potential in an aqueous medium under a heterogeneous condition (Scheme 5C). Anxolabéhère-Mallart and Banse have reported that the reduction of the $Fe^{III}-O_2^{\cdot -}$ species requires ~500 mV greater driving force than that of Fe^{III} porphyrin in organic solvents for both heme and nonheme ligands.[53,64] Hence, the onset potential of ORR for $FeQMe_2$, which does not have an intrinsic proton or electron source, is more cathodic than the $Fe^{III/II}$ E^0. Note that the $Fe^{III}-OOH$ intermediate species, which will be subsequently formed, must be stabilized against hydrolysis to result in a lowering of the PROS formation relative to unfunctionalized porphyrins. Further insight into this is obtained using DFT calculations, vide infra.

Recently published results show that the $FeQH_2$ reduces O_2 all the way to water using two electrons from the iron and two electrons and two protons from the pendant quinol group resulting in the formation of an $Fe^{IV}=O$ quinone species in an organic solvent (Scheme 5A).[37] Here, during a heterogeneous ORR, the same mechanism can be operative, which should result in an onset potential the same as the $Fe^{III/II}$ E^0 as is observed in this investigation. The $Fe^{IV}=O$ and quinone formed during the electrochemical ORR can be reduced back to the ferrous quinol state on the electrode at the potential where ORR is observed (E_{ORR} at −200 mV; the QH_2 to SQ process is observed in the CV at +200 mV). Automatically, such a mechanism will make the ORR intrinsically selective for the $4e^-/4H^+$ reduction of O_2 to water, and this selectivity should be independent of the rate of ET from the electrode as is evidenced from the lack of PROS even at very slow ET rates (Table 1). Because of an alternate mechanism for the O−O bond cleavage, stabilization of an $Fe^{III}-OOH$ may not be important here. Furthermore, the experimental pseudo-first-order rate of ORR observed here is 394 s^{-1} (k_{cat} from K-L analysis × $[O_2]$) for ORR, which, at RT, indicates a barrier of 13.9 kcal/mol, which is very close to the barrier calculated from the previously reported experimentally measured rate-determining second HAT (13.7 kcal/mol) by an $Fe^{III}-OOH$ species from an SQ in an organic solvent.[37]

The ferrous FePh complex reacts with O_2 forming a $Fe^{III}-O_2^{\cdot -}$ species, which rapidly picks up a proton from the pendant phenol and an electron from another ferric superoxide to form an $Fe^{III}-OOH$ species (Scheme 5B) even at −80 °C. The fact that an $Fe^{III}-O_2^{\cdot -}$ can provide the electron needed for the reduction of another $Fe^{III}-O_2^{\cdot -}$ implies that, electrochemically, this ET can be achieved at the same potential where the $Fe^{III}-O_2^{\cdot -}$ is formed, that is, at the potential where Fe^{II} is formed. Hence the $1e^-/1H^+$ PCET reduction of $Fe^{III}-OH$ to $Fe^{II}-OH_2$ under heterogeneous conditions will be rapidly followed by O_2 binding and an ET to reduce $Fe^{III}-O_2^{\cdot -}$ to $Fe^{III}-OOH$ resulting in a $2e^-/1H^+$ PCET as observed here. Thus, the same mechanisms are operative under heterogeneous ORR in aqueous solutions and homogeneous O_2 reduction in an organic solution. The selectivity for $4e^-/4H^+$ ORR is retained by the FePh complex even under slow ET rates suggesting that there must be a mechanism to stabilize the $Fe^{III}-OOH$ species against competitive hydrolysis. This is investigated using DFT calculations below.

4.5. DFT Calculations. Geometry-optimized DFT calculations are used to address the remarkable selectivity of the FePh for $4e^-/4H^+$ even at slow ET rates from the electrode. As discussed earlier, recent SERRS-RDE data show that the PROS are released via the hydrolysis of the $Fe^{III}-OOH$ intermediate produced during ORR. Stabilization of this intermediate or activation of the O−O bond for cleavage results in an enhanced selectivity for $4e^-/4H^+$ ORR. Before the DFT calculations are used to understand these effects, it is used to calculate the relative E^0 for the $Fe^{III/II}$ process to evaluate its accuracy in predicting the properties of these systems.

The $Fe^{III/II}$ process is $1e^-/1H^+$ PCET. Thus, the ΔG for the following reaction is calculated.

$$Fe^{III}-OH + e^- + H^+_{solv} \rightarrow Fe^{II}-OH_2$$

A value of 4.43 eV is used as the value of the free electron, and the free energy of solvation of 271 kcal/mol is assumed for a H^+. Note that both these values are subject to the experimental conditions like the reference electrode used. Hence the relative E^0 values are used normalizing both the DFT-calculated and experimental E^0 of $FeQMe_2$ to be 0 V. The results show a qualitative agreement between the experimental and computed ΔE^0 values (Table 3) justifying the use of the method and basis set for these calculations. These calculations also offer an opportunity to investigate the ~150 mV difference in the E^0 between $FeQMe_2$ and FePh complexes; a difference that is qualitatively reproduced in the calculations as well.

Table 3. Experimental and Theoretical Relative Energies of Ferric and Ferrous Porphyrins

complexes (H bond)	ΔE $Fe^{III/II}$ (mV) (calculated)	ΔE^0 $Fe^{III/II}$ (mV) (observed)
FePh (−OH as H-bond acceptor)	−520	−140
$FeQMe_2$ (−OH as H-bond donor)	0	0
$FeQH_2$ (−OH as H-bond donor)	+30	
$FeQH_2$ (−OH as H-bond acceptor)	−500	−80

The optimized structures of the oxidized ferric state show that the axial OH^- ligand to the iron is hydrogen-bonded to the pendant phenolic groups. While the Fe−OH is a hydrogen-bond acceptor in the FePh and $FeQH_2$ complexes (Figure 8A,E) and the *ortho* hydroxy substituent on the pendant

https://dx.doi.org/10.1021/jacs.0c10385
J. Am. Chem. Soc. XXXX, XXX, XXX−XXX

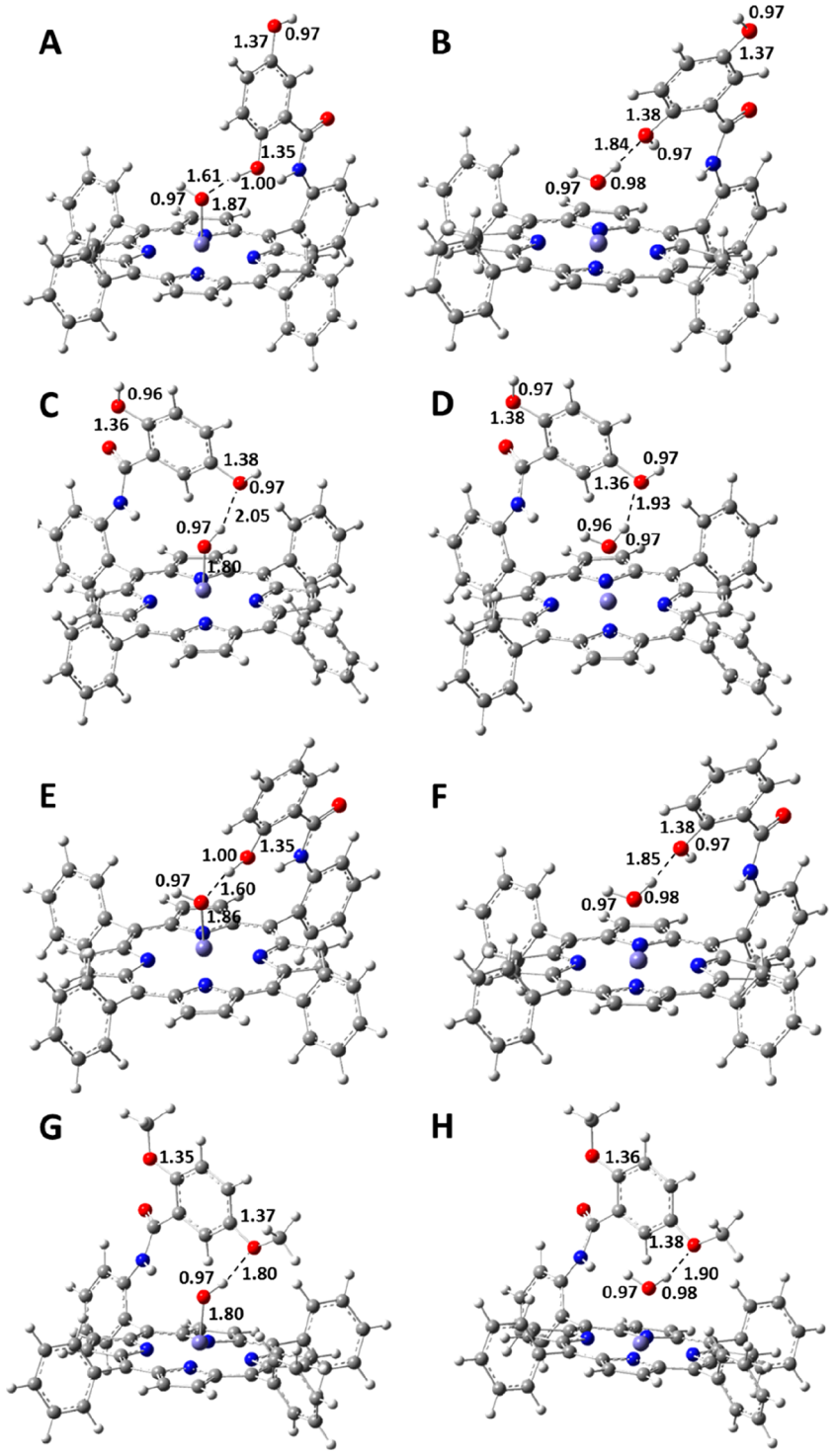

Figure 8. Optimized structure of the ferric hydroxide and ferrous aquo complexes of all the three iron porphyrins. (A) Optimized structure of $Fe^{III}QH_2$−OH with metal-bound hydroxide ligand acting as H-bond acceptor, (B) the optimized structure of the corresponding aquo complex, (C) the optimized structure of $Fe^{III}QH_2$−OH with metal-bound hydroxide complex acting as H-bond donor, (D) the optimized structure of corresponding ferrous aquo complex, (E) the optimized structure of Fe^{III}Ph−OH where the bound hydroxide is a H-bond acceptor, (F) the corresponding ferrous aquo complex, (G) the optimized structure of $FeQMe_2$−OH where the bound hydroxide is a H-bond donor, and (H) the optimized structure of its ferrous aquo complex. The relevant atoms are represented using ball and sticks (color codes are as follows, Fe = purple, O = red, N = blue, C = gray, and H = white), and the porphyrin backbone is represented using thin bonds for clarity.

phenyl ring is the donor (the other geometry for QH_2 higher in energy, Figure 8B), it is a hydrogen-bonding donor in $FeQMe_2$ (Figure 8G) where the *meta* methoxy substituent in the hydrogen-bond acceptor. In the reduced state where the axial ligand is H_2O, the axial H_2O acts as a hydrogen-bonding donor in all three complexes. The reason for the lower potential in FePh and $FeQH_2$ is the greater hydrogen-bonding stabilization of the Fe−OH acceptor *ortho* hydroxy donor orientation over the Fe−OH donor *meta* hydroxy acceptor orientation. The strong hydrogen bonding stabilizes the ferric state of the FePh

https://dx.doi.org/10.1021/jacs.0c10385
J. Am. Chem. Soc. XXXX, XXX, XXX−XXX

and $FeQH_2$ complexes, where this can be achieved due to ability of the ortho-phenolic −OH group to act as a H-bond donor but not in $FeQMe_2$. This observation is further supported by the fact that the calculated E^0 for the model of $FeQH_2$, where the Fe−OH donates H-bond to a pendant hydroquinone (Figure 8C), is ∼530 mV more positive than that of the isomer, where the Fe^{III}−OH acts as a H-bond acceptor (Figure 8A).

Extending these calculations to obtain the hypothetical structures of an Fe^{III}−OOH species, likely to be involved in ORR, one reaches very similar conclusions. The axial OOH^- ligand is hydrogen-bonded in all these complexes (Figure 9A,B). Abiding by the mechanism arrived at experimentally,

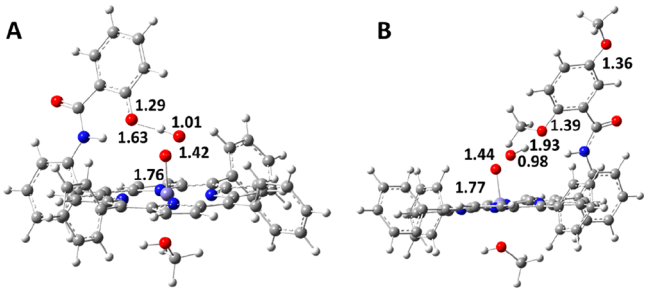

Figure 9. DFT-optimized structure of hydroperoxide-bound (A) FePh and (B) $FeQMe_2$. The atoms are represented using ball and sticks (color codes are as follows, Fe = purple, O = red, N = blue, C = gray, and H = white).

the Fe^{III}−OOH in FePh is hydrogen-bonded to the pendant phenolate. Similarly, the Fe^{III}−OOH is hydrogen-bonded to the pendant SQ in $FeQH_2$ and to the 2,5-dimethoxy phenyl group in $FeQMe_2$. In all these cases the hydrogen bonding is strong, making the species Fe^{III}−OOH resistant toward hydrolysis-reducing PROS. This is consistent with the experimental data, where the selectivity for $4e^-/4H^+$ ORR is retained even under very slow ET in sharp contrast to iron porphyrins without such a preorganized hydrogen-bonding network, where as much as 50−100% H_2O_2 has been reported.[25,28] The DFT calculations further show that the H-bonding distance between the bound −OOH ligand and pendant phenolate oxygen is 1.63 Å, while in the case of $FeQMe_2$ the H-bonding distance between Fe bound −OOH and phenyl −OMe group is 1.93 Å (Figure 9). Thus, the hydrogen bonding of the bound hydroperoxide is much stronger with the pendant phenolate than it is with the methoxy group, which explains why the $FeQMe_2$ complex produces more PROS than the FePh complex when the electron transfer from the electrode is slow. Note that the $FeQH_2$ complex is primed for a facile HAT by the Fe^{III}−OOH moiety, which would naturally bias the selectivity toward $4e^-/4H^+$.

5. DISCUSSION

Three Fe porphyrins bearing pendant phenol, hydroquinone, and a 2,5-dimethoxyphenyl ring are investigated. Under a heterogeneous condition in aqueous medium all three mononuclear Fe porphyrins reduce O_2 electrochemically to H_2O with very high selectivity and with almost the same second-order rate constant when the catalysts are physiad-sorbed on edge plane graphite electrode, where the ET to the catalytic center is facile. Under heterogeneous conditions, the ORR catalyzed by $FeQMe_2$ proceeds at −130 mV more cathodic potential than its $Fe^{III/II}$ potential. This is because the reduction of the Fe^{III}−$O_2^{\cdot -}$ species to produce water requires electrons to be supplied by the electrode to it, and the reaction follows an ETPT pathway to form ferric hydroperoxide in an aqueous medium (Scheme 5C). The $FeQH_2$ complex follows a consecutive HAT pathway during an oxygen reduction reaction in organic medium involving an Fe^{III}−$O_2^{\cdot -}$-QH_2 species, Fe^{III}−OOH-SQ species, and Fe^{IV}-oxo-Q intermediates (Scheme 5A), which have been characterized using UV−vis, EPR, and resonance Raman spectroscopy previously.[37] Thus, of the four electrons required for the reduction of oxygen to water, two are supplied by ferrous porphyrin, which is oxidized to a ferryl species, and the rest are supplied by a distal hydroquinone group, which is oxidized to quinone at the end of the reaction. Here a 60 mV/pH shift in the E_{ORR} potential, which overlays the $E^{1/2}$ measured at these pH values, implies that the potential determining step of ORR involves a $1H^+/1e^-$ PCET reduction of Fe^{III}−OH to $Fe^{II}OH_2$ as is expected based on the previous results obtained in an organic medium. Furthermore, the pseudo-first-order rate constant of an oxygen reduction reaction in an aqueous medium is found to be 394 s^{-1}, which is similar to the rate of the slow second HAT step found in an organic medium. Thus, the consecutive HAT pathway is likely operative during ORR by $FeQH_2$ both in an aqueous medium as well as in an organic medium. When hydroquinone is replaced with phenol in FePh, the Fe^{III}−$O_2^{\cdot -}$ species formed in solution does not abstract a H atom from a pendant phenol residue unlike $FeQH_2$. Rather in the case of FePh a ferric superoxide complex is reduced to a low-spin ferric hydroperoxide intermediate via a PCET mechanism, where a proton comes from a pendant phenol, and the electron is donated by another Fe^{III}−$O_2^{\cdot -}$ species (Scheme 5B). During a heterogeneous oxygen reduction in aqueous medium FePh follows a $1H^+/2e^-$ PCET pathway, where the potential determining step for ORR is the reduction of Fe^{III}−OH to Fe^{II}−H_2O followed by rapid oxygen binding to ferrous porphyrin and a second electron transfer resulting in the reduction of a ferric superoxide species to form a ferric peroxide species. The fact that the ferric superoxide formed on the electrode during ORR can be rapidly reduced to the ferric hydroperoxide at the same potential is consistent with the fact that an analogous ferric superoxide formed in solution can be reduced by another ferric superoxide ($\Delta G \approx 0$) via PCET. Thus, the FePh complex follows a PCET pathway to reduce oxygen to water both in organic solvent as well as in aqueous medium (Scheme 5B).

The DFT calculations reveal that the HAT process for FePh (ΔG = +12.2 kcal/mol) is more energy demanding than that for $FeQH_2$ (ΔG = +3.9 kcal/mol). The bond dissociation energy (BDE) of the O−H bond of phenol and hydroquinone calculated using equation iii shows that the BDE of phenol (BDE_{O-H} = 87 kcal/mol) is ∼6−7 kcal/mol higher compared to that of the hydroquinone (BDE_{O-H} = 80 kcal/mol).[65] This is probably because of the higher redox potential of the RO·/RO^- redox couple and lower pK_a of phenol compared to hydroquinone. In aqueous solution in neutral pH the reduction potential of phenol (∼0.8 V) is much higher than that of hydroquinone (∼0.46 V).[65] Furthermore, the pK_a of the phenol in an aqueous medium is 9.98, while that of hydroquinone is 11.4.[66] Please note that, while the absolute values of pK_a and E^0 will be different in these substituted

https://dx.doi.org/10.1021/jacs.0c10385
J. Am. Chem. Soc. XXXX, XXX, XXX−XXX

phenols and quinols relative to free phenols and quinol, the relative values are likely to be the same.

$$BDE_{OH} = C_H + 1.37pk_a + 23.06 \times E^0 \quad \text{(iii)}$$

where C_H represents the enthalpic constant and includes the free energy of formation of a hydrogen radical, free energy of solvation of hydrogen radical in the solvent, and an entropy term.

Thus the higher BDE of the O−H bond of phenol compared to that of hydroquinone prevents the ferric superoxide of FePh from abstracting a H atom from the pendant phenol group; rather, it chooses a different mechanism involving a concerted proton-coupled electron transfer pathway. The high endothermicity of an HAT process in FePh relative to $FeQH_2$ in the superoxide adduct of FePh should increase the energy of the corresponding transition state ~12 kcal/mol higher than ~13.4 kcal/mol calculated for the $FeQH_2$ complex (Figure 10)

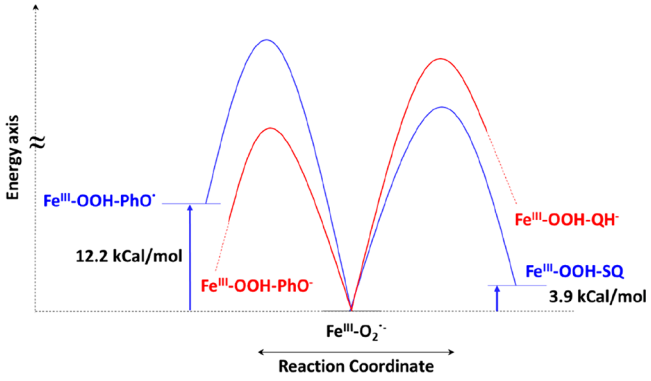

Figure 10. Energy profile diagram for an HAT and PCET reaction involved in the conversion from ferric heme superoxide to ferric heme hydroperoxide complex for $FeQH_2$ and FePh.

Alternatively, for the $Fe^{III}-O_2^{\cdot-}$ adduct of the FePh complex, which has a high barrier for HAT owing to the high BDE_{OH} of PhOH, PCET is a more favored reaction. A PCET to an $Fe^{III}-O_2^{\cdot-}$ can be viewed as a reduction of this species followed by a proton transfer from the pendant phenol or quinol groups. The overall energy of this process can be expressed as

$$\Delta G_{PCET} = \Delta G_{ET} + \Delta G_{PT}$$

where ΔG_{ET} represents the free energy of reduction of the $Fe^{III}-O_2^{\cdot-}$ species by the reductant in solution, and ΔG_{PT} represents the free energy of proton transfer from the pendant phenol/quinol to the $Fe^{III}-O_2^{2-}$ species formed. The ΔG_{ET} is almost 0 for both the complexes, and the optimized structure (Figure 11) of the resultant $Fe^{III}-OOH$ is almost identical for both FePh and $FeQH_2$. The only difference is in the heterolytic bond dissociation energies of the phenolic and the quinolic −OH groups. This is reflected in their pK_a values. The pK_a of quinol is ~1.42 unit greater than that of phenol, which translates to 1.94 kcal/mol higher proton transfer energy for the $FeQH_2$ complex relative to the FePh complex. Thus, the PCET to an $Fe^{III}-O_2^{\cdot-}$ species should be favorable in the FePh complex by 1.94 kcal/mol relative to the $FeQH_2$ complex. Recent results on synthetic heme/Cu systems suggest that the H-bonding interaction with the acidic proton of a phenol can help to polarize the O−O bond of a bridging peroxide, where a proton and electron are transferred from the

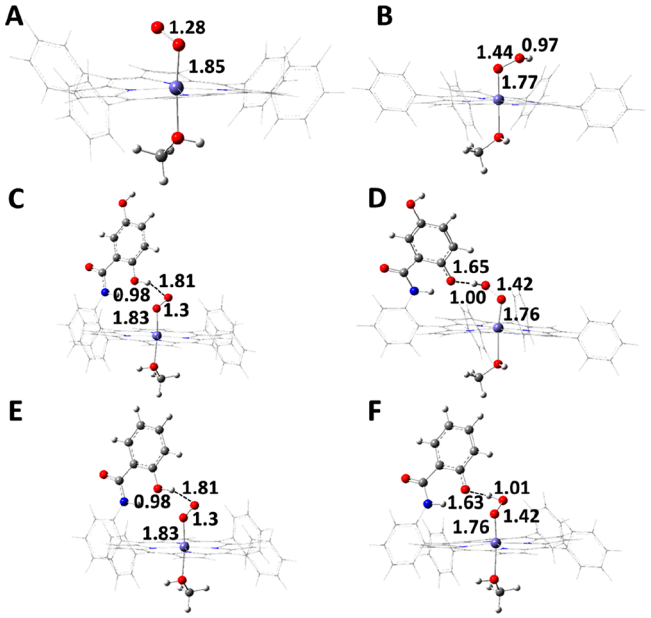

Figure 11. DFT-optimized structure of ferric superoxide and ferric hydroperoxide complexes, which are proposed to form after PCET to the precursor $Fe^{III}-O_2^{\cdot-}$ complexes of FeTPP (A, B), $FeQH_2$ (C, D), and FePh (E, F). The relevant atoms are represented using ball and sticks (color codes are as follows, Fe = purple, O = red, N = blue, C = gray and H = white), and the porphyrin backbone is represented as wire for clarity.

phenol.[18] The results presented here show that a suitably placed phenol with a proton with a low pK_a can enable a facile PCET in an $Fe^{III}-O_2^{\cdot-}$ species as well.

Finally, the FeTPP-$O_2^{\cdot-}$ complex does not show PCET when reacted with external PhOH despite having the same ΔG_{PCET} as the FePh-$O_2^{\cdot-}$ species. The optimized structures of the reactant $Fe^{III}-O_2^{\cdot-}$ and product $Fe^{III}-OOH$ of FeTPP, FePh, and $FeQH_2$ show that the O−O bond length of $Fe^{III}-O_2^{\cdot-}$ is shorter, while that for $Fe^{III}-OOH$ is longer for FeTPP relative to both FePh and $FeQH_2$ (Table 4). The $Fe^{III}-O_2^{\cdot-}$ adducts of both FePh and $FeQH_2$ have pendant hydroxyl groups, which act as hydrogen-bond donor to the bound superoxide. The polarization of the electron density on the superoxide by the hydroxyl groups in FePh and $FeQH_2$ lead to elongation of the O−O bond (Table 4). Similarly, the deprotonated phenolate and quinolate oxygen act as hydrogen-bond acceptor to the bound hydroperoxide of the $Fe^{III}-OOH$ species. This hydrogen bonding leads to an increased electron density on the bound hydroperoxide leading to a shorter O−O distance in these hydrogen-bonded $Fe^{III}-OOH$ species (Table 4). Overall, the hydrogen bonding between the pendant phenol/quinol in the reactant $Fe^{III}-O_2^{\cdot-}$ species makes the O−O bond longer, whereas hydrogen bonding between the phenolate/quinolate with $Fe^{III}-OOH$ in the product makes the O−O bond shorter, which is responsible for the smaller displacement in the O−O bond during the PCET reaction for FePh/$FeQH_2$ compared to FeTPP.

The inner-sphere reorganization energy ($\lambda_{inner\text{-}sphere}$) for an ET process can be expressed as $\Sigma k_i(x_i)^2$, where k_i is calculated from the individual force constant of the bonds involved in the ith normal mode both for the reactant and product molecules using eqs va, vb, and vc, and x_i is the change of equilibrium bond length between reactant and product along the ith normal mode. The individual force constant (f) of any

https://dx.doi.org/10.1021/jacs.0c10385
J. Am. Chem. Soc. XXXX, XXX, XXX−XXX

Table 4. Calculated Bond Lengths (Å) and Stretching Frequencies (cm^{-1}) of the Reactant and Products That Are Supposed to Be Involved in the PCET Process

	ferric-$O_2^{\cdot -}$-ROH						ferric-OOH-RO^-					
	Fe−O bond		O−O bond		O−H bond		Fe−O bond		O−O bond		O−H bond	
complex	length (Å)	ν_{Fe-O} (cm^{-1})	length (Å)	ν_{O-O} (cm^{-1})	length (Å)	ν_{O-H} (cm^{-1})	length (Å)	ν_{Fe-O} (cm^{-1})	length (Å)	ν_{O-O} (cm^{-1})	length (Å)	ν_{O-H} (cm^{-1})
FeTPP	1.85	502	1.28	1244	0.97	3731	1.77	655	1.44	907	0.97	3672
$FeQH_2$	1.83	559	1.30	1246	0.98	3476	1.76	661	1.42	948	1.00	3129
FePh	1.83	562	1.30	1244	0.98	3463	1.76	674	1.42	944	1.01	2987
FePh-$3H_2O$	1.84	545	1.31	1241	0.98	3527	1.79	622	1.44	902	1.0	3090

particular bond is calculated from its stretching frequency (ν) and reduced mass (μ) using eq iv.[67,68]

$$\nu = (1/(2\pi c)) \times (f/\mu)^{1/2}$$

$$f_{Fe\text{-}O}{}^{hyd} = (2\pi c)^2 \times \mu \times \nu_{Fe\text{-}O}{}^{hyd})^2 \quad \text{(iv)}$$

$$k_{Fe\text{-}O} = (f_{Fe\text{-}O}{}^{hyd} \times f_{Fe\text{-}O}{}^{sup})/(f_{Fe\text{-}O}{}^{hyd} + f_{Fe\text{-}O}{}^{sup}) = ((2\pi c)^2 \times \mu \times ((\nu_{Fe\text{-}O}{}^{hyd})^2 \times (\nu_{Fe\text{-}O}{}^{sup})^2) /((\nu_{Fe\text{-}O}{}^{hyd})^2 + (\nu_{Fe\text{-}O}{}^{sup})^2) \quad \text{(va)}$$

$$k_{O\text{-}O} = (f_{O\text{-}O}{}^{hyd} \times f_{O\text{-}O}{}^{sup})/(f_{O\text{-}O}{}^{hyd} + f_{O\text{-}O}{}^{sup}) = ((2\pi c)^2 \times \mu \times ((\nu_{O\text{-}O}{}^{hyd})^2 \times (\nu_{O\text{-}O}{}^{sup})^2) /((\nu_{O\text{-}O}{}^{hyd})^2 + (\nu_{O\text{-}O}{}^{sup})^2) \quad \text{(vb)}$$

$$k_{O\text{-}H} = (f_{O\text{-}H}{}^{hyd} \times f_{O\text{-}H}{}^{ROH})/(f_{O\text{-}H}{}^{hyd} + f_{O\text{-}H}{}^{ROH}) = ((2\pi c)^2 \times \mu \times ((\nu_{O\text{-}H}{}^{hyd})^2 \times (\nu_{O\text{-}H}{}^{ROH})^2) /((\nu_{O\text{-}H}{}^{hyd})^2 + (\nu_{O\text{-}H}{}^{ROH})^2) \quad \text{(vc)}$$

$$\lambda_{inner\text{-}sphere} = \sum k_i x_i{}^2 = k_{Fe\text{-}O}(d_{Fe\text{-}O}{}^{hyd} - d_{Fe\text{-}O}{}^{sup})^2 + k_{O\text{-}O}(d_{O\text{-}O}{}^{hyd} - d_{O\text{-}O}{}^{sup})^2 + k_{O\text{-}H}(d_{O\text{-}H}{}^{hyd} - d_{O\text{-}H}{}^{ROH})^2 \quad \text{(vi)}$$

The computed $\lambda_{inner\text{-}sphere}$ for a PCET process suggests that both $FeQH_2$ and FePh have a comparable $\lambda_{inner\text{-}sphere}$ for the PCET process and that the values are sufficiently lower than that of the FeTPP. The O−O bond is strong with a force constant of 7.29 mdyne/Å for a superoxide and 3.87 mdyne/Å for a hydroperoxide of FeTPP. As a result, the $\lambda_{inner\text{-}sphere}$ is dominated by the contribution from the elongation of the O−O both from Fe^{III}−$O_2^{\cdot -}$ to Fe^{III}−OOH. While the O−H bond has a higher force constant, its contribution to the $\lambda_{inner\text{-}sphere}$ is negligible due to a smaller change in the O−H bond length between the product Fe^{III}−OOH and the reactant PhOH/QH_2 (Table 4). Given that the $\lambda_{inner\text{-}sphere}$ varies with the square of the displacement, a lower displacement of the O−O bond results in a lower $\lambda_{inner\text{-}sphere}$ in the FePh/$FeQH_2$ complex compared to FeTPP. Thus, the strong interaction with the pendant phenol/hydroquinone is quintessential for lowering the $\lambda_{inner\text{-}sphere}$ for PCET in FePh/$FeQH_2$ relative to FeTPP by ∼3 kcal/mol making the process more favorable in the complexes bearing hydrogen bonding in the distal site promoted by the pendant groups.

$$\lambda_{inner\text{-}sphere}{}^{FeQH2} = k_{Fe\text{-}O}(d_{Fe\text{-}O}{}^{hyd} - d_{Fe\text{-}O}{}^{sup})^2 + k_{O\text{-}O}(d_{O\text{-}O}{}^{hyd} - d_{O\text{-}O}{}^{sup})^2 + k_{O\text{-}H}(d_{O\text{-}H}{}^{hyd} - d_{O\text{-}H}{}^{ROH})^2 = 3941.89 + 24\,586.85 + 722.63 = 29.2 \text{ kJ/mol} = 6.98 \text{ kcal/mol}$$

$$\lambda_{inner\text{-}sphere}{}^{FePh} = k_{Fe\text{-}O}(d_{Fe\text{-}O}{}^{hyd} - d_{Fe\text{-}O}{}^{sup})^2 + k_{O\text{-}O}(d_{O\text{-}O}{}^{hyd} - d_{O\text{-}O}{}^{sup})^2 + k_{O\text{-}H}(d_{O\text{-}H}{}^{hyd} - d_{O\text{-}H}{}^{ROH})^2 = 4390.92 + 25\,483.93 + 1538.558 = 31.4 \text{ kJ/mol} = 7.5 \text{ kcal/mol}$$

$$\lambda_{inner\text{-}sphere}{}^{FeTPP} = k_{Fe\text{-}O}(d_{Fe\text{-}O}{}^{hyd} - d_{Fe\text{-}O}{}^{sup})^2 + k_{O\text{-}O}(d_{O\text{-}O}{}^{hyd} - d_{O\text{-}O}{}^{sup})^2 + k_{O\text{-}H}(d_{O\text{-}H}{}^{hyd} - d_{O\text{-}H}{}^{ROH})^2 = 4485.61 + 39\,536.21 + 54.70 = 44.07 \text{ kJ/mol} = 10.53 \text{ kcal/mol}$$

$$\lambda_{inner\text{-}sphere}{}^{FePh\text{-}H2O} = k_{Fe\text{-}O}(d_{Fe\text{-}O}{}^{hyd} - d_{Fe\text{-}O}{}^{sup})^2 + k_{O\text{-}O}(d_{O\text{-}O}{}^{hyd} - d_{O\text{-}O}{}^{sup})^2 + k_{O\text{-}H}(d_{O\text{-}H}{}^{hyd} - d_{O\text{-}H}{}^{ROH})^2 = 1859.48 + 29\,238.16 + 721.96 = 31.8 \text{ kJ/mol} = 7.6 \text{ kcal/mol}$$

The $\lambda_{inner\text{-}sphere}$ in FeTPP-O_2^- is thus 3 kcal/mol higher than $\lambda_{inner\text{-}sphere}$ in FePh-$O_2^{\cdot -}$ and $FeQH_2$−$O_2^{\cdot -}$ making the PCET substantially unfavorable in the former. These estimates indicate a clear advantage of having hydrogen bonding in lowering the $\lambda_{inner\text{-}sphere}$ for the PCET from Fe^{III}−$O_2^{\cdot -}$ to Fe^{III}−OOH. The H bonding between the distal superoxide and hydroperoxide with distal residues may or may not be retained in an aqueous medium, where these experiments are performed. To validate this DFT optimization was performed on ferric superoxide and hydroperoxide complexes of FePh with three water molecules in the distal pocket (Figure S18). The optimized geometries and calculated frequencies are very similar to the parent FePh complex (Table 4, rows 3 and 4). In particular, the critical differences in the O−O bond lengths upon reduction are retained even when three explicit water molecules are added. As a result, the inner-sphere reorganization energy for the conversion of ferric-hydroperoxide complexes from the ferric-superoxide complexes calculated from the optimized structure and frequencies is found to be

https://dx.doi.org/10.1021/jacs.0c10385
J. Am. Chem. Soc. XXXX, XXX, XXX−XXX

very similar to that of the FePh without external water molecules in the distal pocket. This suggests that the effect of a distal residue on the mechanism of conversion of ferric hydroperoxide from a ferric superoxide complex may not alter substantially with a change in the solvent from organic to aqueous.

6. SUMMARY

The electrocatalytic ORR by three structurally analogous iron porphyrin complexes bearing phenol, quinol, and methylquinone groups and their reactivities in solution with O_2 show that the mechanism of O_2 reduction can vary dramatically, even though their apparent rates and selectivity for ORR are similar under certain conditions. Probing the electrochemical ORR under different pH values and electron transfer rates reveals very different mechanisms of ORR at play. Simultaneous investigations of an O_2 reaction in homogeneous conditions help to further confirm the differences in the mechanism. A pendant methylquinone group can restrain the hydrolysis of an Fe^{III}–OOH group offering good selectivity for $4e^-/4H^+$ ORR via an ETPT pathway only when the ET from the electrode is fast. The low reduction potential of a quinol allows the iron porphyrin complex with a pendant quinol to reduce O_2 via two consecutive HATs to an Fe^{III}–$O_2^{\cdot -}$ adduct. This pathway is inaccessible when the quinol is replaced by a phenol due to the high reduction potential of the phenol. Rather the low pK_a (greater acidity) of the pendant phenol allows ORR via a favorable PCET to this Fe^{III}–$O_2^{\cdot -}$ species. The advantages of a pendant phenol or quinol are (a) prearranged favorable orientation of the Fe^{III}–$O_2^{\cdot -}$ and the H atom/proton source, (b) lowering of λ for the PCET from Fe^{III}–$O_2^{\cdot -}$ to Fe^{III}–OOH, and (c) stabilization the Fe^{III}–OOH intermediate by hydrogen bonding (evidenced by its detection in organic solutions), which helps these complexes retain more than 95% selectivity for $4e^-/4H^+$ ORR even under very slow ET flux from the electrode.

■ ASSOCIATED CONTENT

Supporting Information

The Supporting Information is available free of charge at https://pubs.acs.org/doi/10.1021/jacs.0c10385.

^{1}H NMR data of the ligands, ESI-MS of the ligands and the complexes, additional spectroscopic data, and optimized coordinates (PDF)

X-ray crystallographic information (CIF)

■ AUTHOR INFORMATION

Corresponding Author

Abhishek Dey − *School of Chemical Science, Indian Association for the Cultivation of Science, Kolkata 700032, India;* orcid.org/0000-0002-9166-3349; Email: icad@iacs.res.in

Authors

Asmita Singha − *School of Chemical Science, Indian Association for the Cultivation of Science, Kolkata 700032, India;* orcid.org/0000-0001-5512-253X

Arnab Mondal − *School of Chemical Science, Indian Association for the Cultivation of Science, Kolkata 700032, India*

Abhijit Nayek − *School of Chemical Science, Indian Association for the Cultivation of Science, Kolkata 700032, India;* orcid.org/0000-0001-9981-4271

Somdatta Ghosh Dey − *School of Chemical Science, Indian Association for the Cultivation of Science, Kolkata 700032, India;* orcid.org/0000-0002-6142-2202

Complete contact information is available at: https://pubs.acs.org/10.1021/jacs.0c10385

Notes

The authors declare no competing financial interest.

■ ACKNOWLEDGMENTS

The research is funded by Department of Science and Technology (SERB) Grant No. EMR-0008063.

■ REFERENCES

(1) Ferguson-Miller, S.; Babcock, G. T. Heme/Copper Terminal Oxidases. *Chem. Rev.* **1996**, *96*, 2889−2908.

(2) Proshlyakov, D. A.; Pressler, M. A.; Babcock, G. T. Dioxygen activation and bond cleavage by mixed-valence cytochrome c oxidase. *Proc. Natl. Acad. Sci. U. S. A.* **1998**, *95*, 8020.

(3) Yoshikawa, S.; Shinzawa-Itoh, K.; Nakashima, R.; Yaono, R.; Yamashita, E.; Inoue, N.; Yao, M.; Fei, M. J.; Libeu, C. P.; Mizushima, T.; Yamaguchi, H.; Tomizaki, T.; Tsukihara, T. Redox-Coupled Crystal Structural Changes in Bovine Heart Cytochrome c Oxidase. *Science* **1998**, *280*, 1723.

(4) Proshlyakov, D. A.; Pressler, M. A.; DeMaso, C.; Leykam, J. F.; DeWitt, D. L.; Babcock, G. T. Oxygen Activation and Reduction in Respiration: Involvement of Redox-Active Tyrosine 244. *Science* **2000**, *290*, 1588.

(5) Morgan, J. E.; Verkhovsky, M. I.; Wikström, M. Observation and Assignment of Peroxy and Ferryl Intermediates in the Reduction of Dioxygen to Water by Cytochrome c Oxidase. *Biochemistry* **1996**, *35*, 12235−12240.

(6) Yoshikawa, S.; Shimada, A. Reaction Mechanism of Cytochrome c Oxidase. *Chem. Rev.* **2015**, *115*, 1936−1989.

(7) Babcock, G. T. How oxygen is activated and reduced in respiration. *Proc. Natl. Acad. Sci. U. S. A.* **1999**, *96*, 12971.

(8) Collman, J. P.; Boulatov, R.; Sunderland, C. J.; Fu, L. Functional Analogues of Cytochrome c Oxidase, Myoglobin, and Hemoglobin. *Chem. Rev.* **2004**, *104*, 561−588.

(9) Amanullah, S.; Singha, A.; Dey, A. Tailor made iron porphyrins for investigating axial ligand and distal environment contributions to electronic structure and reactivity. *Coord. Chem. Rev.* **2019**, *386*, 183−208.

(10) Collman, J. P.; Rapta, M.; Bröring, M.; Raptova, L.; Schwenninger, R.; Boitrel, B.; Fu, L.; L'Her, M. Close Structural Analogues of the Cytochrome c Oxidase Fea3/CuB Center Show Clean 4e- Electroreduction of O2 to H2O at Physiological pH. *J. Am. Chem. Soc.* **1999**, *121*, 1387−1388.

(11) Collman, J. P.; Sunderland, C. J.; Berg, K. E.; Vance, M. A.; Solomon, E. I. Spectroscopic Evidence for a Heme−Superoxide/Cu(I) Intermediate in a Functional Model of Cytochrome c Oxidase. *J. Am. Chem. Soc.* **2003**, *125*, 6648−6649.

(12) Sasaki, T.; Nakamura, N.; Naruta, Y. Formation and Spectroscopic Characterization of the PeroxoFeIII-CuII Complex. A Modeling Reaction of the Heme-Cu Site in Cytochrome c Oxidase. *Chem. Lett.* **1998**, *27*, 351−352.

(13) Chufán, E. E.; Karlin, K. D. An Iron−Peroxo Porphyrin Complex: New Synthesis and Reactivity Toward a Cu(II) Complex Giving a Heme−Peroxo−Copper Adduct. *J. Am. Chem. Soc.* **2003**, *125*, 16160−16161.

(14) Chishiro, T.; Shimazaki, Y.; Tani, F.; Tachi, Y.; Naruta, Y.; Karasawa, S.; Hayami, S.; Maeda, Y. Isolation and Crystal Structure of a Peroxo-Bridged Heme−Copper Complex. *Angew. Chem., Int. Ed.* **2003**, *42*, 2788−2791.

(15) Ghiladi, R. A.; Hatwell, K. R.; Karlin, K. D.; Huang, H.-w.; Moënne-Loccoz, P.; Krebs, C.; Huynh, B. H.; Marzilli, L. A.; Cotter, R. J.; Kaderli, S.; Zuberbühler, A. D. Dioxygen Reactivity of Mononuclear Heme and Copper Components Yielding A High-Spin Heme−Peroxo−Cu Complex. *J. Am. Chem. Soc.* **2001**, *123*, 6183−6184.
(16) Ghiladi, R. A.; Chufán, E. E.; del Río, D.; Solomon, E. I.; Krebs, C.; Huynh, B. H.; et al. Further Insights into the Spectroscopic Properties, Electronic Structure, and Kinetics of Formation of the Heme−Peroxo−Copper Complex [(F8TPP)FeIII−(O22-)−CuII-(TMPA)]+. *Inorg. Chem.* **2007**, *46*, 3889−3902.
(17) Collman, J. P.; Decréau, R. A.; Yan, Y.; Yoon, J.; Solomon, E. I. Intramolecular Single-Turnover Reaction in a Cytochrome c Oxidase Model Bearing a Tyr244 Mimic. *J. Am. Chem. Soc.* **2007**, *129*, 5794−5795.
(18) Schaefer, A. W.; Kieber-Emmons, M. T.; Adam, S. M.; Karlin, K. D.; Solomon, E. I. Phenol-Induced O−O Bond Cleavage in a Low-Spin Heme−Peroxo−Copper Complex: Implications for O2 Reduction in Heme−Copper Oxidases. *J. Am. Chem. Soc.* **2017**, *139*, 7958−7973.
(19) Collman, J. P.; Devaraj, N. K.; Decréau, R. A.; Yang, Y.; Yan, Y.-L.; Ebina, W.; Eberspacher, T. A.; Chidsey, C. E. D. A Cytochrome c Oxidase Model Catalyzes Oxygen to Water Reduction Under Rate-Limiting Electron Flux. *Science* **2007**, *315*, 1565.
(20) Halime, Z.; Kieber-Emmons, M. T.; Qayyum, M. F.; Mondal, B.; Gandhi, T.; Puiu, S. C.; Chufán, E. E.; Sarjeant, A. A. N.; Hodgson, K. O.; Hedman, B.; Solomon, E. I.; Karlin, K. D. Heme−Copper−Dioxygen Complexes: Toward Understanding Ligand-Environmental Effects on the Coordination Geometry, Electronic Structure, and Reactivity. *Inorg. Chem.* **2010**, *49*, 3629−3645.
(21) Kieber-Emmons, M. T.; Li, Y.; Halime, Z.; Karlin, K. D.; Solomon, E. I. Electronic Structure of a Low-Spin Heme/Cu Peroxide Complex: Spin-State and Spin-Topology Contributions to Reactivity. *Inorg. Chem.* **2011**, *50*, 11777−11786.
(22) Kieber-Emmons, M. T.; Qayyum, M. F.; Li, Y.; Halime, Z.; Hodgson, K. O.; Hedman, B.; Karlin, K. D.; Solomon, E. I. Spectroscopic Elucidation of a New Heme/Copper Dioxygen Structure Type: Implications for O···O Bond Rupture in Cytochrome c Oxidase. *Angew. Chem., Int. Ed.* **2012**, *51*, 168−172.
(23) Kim, H.; Sharma, S. K.; Schaefer, A. W.; Solomon, E. I.; Karlin, K. D. Heme−Cu Binucleating Ligand Supports Heme/O2 and FeII−CuI/O2 Reactivity Providing High- and Low-Spin FeIII−Peroxo−CuII Complexes. *Inorg. Chem.* **2019**, *58*, 15423−15432.
(24) Schaefer, A. W.; Ehudin, M. A.; Quist, D. A.; Tang, J. A.; Karlin, K. D.; Solomon, E. I. Spin Interconversion of Heme-Peroxo-Copper Complexes Facilitated by Intramolecular Hydrogen-Bonding Interactions. *J. Am. Chem. Soc.* **2019**, *141*, 4936−4951.
(25) Rigsby, M. L.; Wasylenko, D. J.; Pegis, M. L.; Mayer, J. M. Medium Effects Are as Important as Catalyst Design for Selectivity in Electrocatalytic Oxygen Reduction by Iron−Porphyrin Complexes. *J. Am. Chem. Soc.* **2015**, *137*, 4296−4299.
(26) McGuire, R., Jr; Dogutan, D. K.; Teets, T. S.; Suntivich, J.; Shao-Horn, Y.; Nocera, D. G. Oxygen reduction reactivity of cobalt(ii) hangman porphyrins. *Chemical Science* **2010**, *1*, 411−414.
(27) Samanta, S.; Mittra, K.; Sengupta, K.; Chatterjee, S.; Dey, A. Second Sphere Control of Redox Catalysis: Selective Reduction of O2 to O2− or H2O by an Iron Porphyrin Catalyst. *Inorg. Chem.* **2013**, *52*, 1443−1453.
(28) Collman, J. P.; Decréau, R. A.; Lin, H.; Hosseini, A.; Yang, Y.; Dey, A.; Eberspacher, T. A. Role of a distal pocket in the catalytic O2 reduction by cytochrome c oxidase models immobilized on interdigitated array electrodes. *Proc. Natl. Acad. Sci. U. S. A.* **2009**, *106*, 7320.
(29) Sengupta, K.; Chatterjee, S.; Samanta, S.; Dey, A. Direct observation of intermediates formed during steady-state electrocatalytic O2 reduction by iron porphyrins. *Proc. Natl. Acad. Sci. U. S. A.* **2013**, *110*, 8431.
(30) Mukherjee, S.; Mukherjee, A.; Bhagi-Damodaran, A.; Mukherjee, M.; Lu, Y.; Dey, A. A biosynthetic model of cytochrome c oxidase as an electrocatalyst for oxygen reduction. *Nat. Commun.* **2015**, *6*, 8467.
(31) Chatterjee, S.; Sengupta, K.; Hematian, S.; Karlin, K. D.; Dey, A. Electrocatalytic O2-Reduction by Synthetic Cytochrome c Oxidase Mimics: Identification of a "Bridging Peroxo" Intermediate Involved in Facile 4e−/4H+ O2-Reduction. *J. Am. Chem. Soc.* **2015**, *137*, 12897−12905.
(32) Sengupta, K.; Chatterjee, S.; Dey, A. Catalytic H2O2 Disproportionation and Electrocatalytic O2 Reduction by a Functional Mimic of Heme Catalase: Direct Observation of Compound 0 and Compound I in Situ. *ACS Catal.* **2016**, *6*, 1382−1388.
(33) Mukherjee, S.; Bandyopadhyay, S.; Chatterjee, S.; Dey, A. Electrocatalytic O2 reduction by a monolayer of hemin: the role of pKa of distal and proximal oxygen of a FeIII−OOH species in determining reactivity. *Chem. Commun.* **2014**, *50*, 12304−12307.
(34) Chatterjee, S.; Sengupta, K.; Samanta, S.; Das, P. K.; Dey, A. Concerted Proton−Electron Transfer in Electrocatalytic O_2 Reduction by Iron Porphyrin Complexes: Axial Ligands Tuning H/D Isotope Effect. *Inorg. Chem.* **2015**, *54*, 2383−2392.
(35) Bhunia, S.; Rana, A.; Roy, P.; Martin, D. J.; Pegis, M. L.; Roy, B.; Dey, A. Rational Design of Mononuclear Iron Porphyrins for Facile and Selective $4e^-/4H^+$ O_2 Reduction: Activation of O−O Bond by 2nd Sphere Hydrogen Bonding. *J. Am. Chem. Soc.* **2018**, *140*, 9444−9457.
(36) Bhunia, S.; Rana, A.; Dey, S. G.; Ivancich, A.; Dey, A. A designed second-sphere hydrogen-bond interaction that critically influences the O−O bond activation for heterolytic cleavage in ferric iron−porphyrin complexes. *Chem. Sci.* **2020**, *11*, 2681.
(37) Singha, A.; Dey, A. Hydrogen atom abstraction by synthetic heme ferric superoxide and hydroperoxide species. *Chem. Commun.* **2019**, *55*, 5591−5594.
(38) Kim, H.; Rogler, P. J.; Sharma, S. K.; Schaefer, A. W.; Solomon, E. I.; Karlin, K. D. Heme-FeIII Superoxide, Peroxide and Hydroperoxide Thermodynamic Relationships: FeIII-O2•− Complex H-Atom Abstraction Reactivity. *J. Am. Chem. Soc.* **2020**, *142*, 3104−3116.
(39) Mukherjee, M.; Dey, A. Catalytic C−H Bond Oxidation Using Dioxygen by Analogues of Heme Superoxide. *Inorg. Chem.* **2020**, *59*, 7415−7425.
(40) Mondal, P.; Wijeratne, G. B. Modeling Tryptophan/Indoleamine 2,3-Dioxygenase with Heme Superoxide Mimics: Is Ferryl the Key Intermediate? *J. Am. Chem. Soc.* **2020**, *142*, 1846−1856.
(41) Sarewicz, M.; Osyczka, A. Electronic Connection Between the Quinone and Cytochrome c Redox Pools and Its Role in Regulation of Mitochondrial Electron Transport and Redox Signaling. *Physiol. Rev.* **2015**, *95*, 219−243.
(42) Cramer, W. A.; Hasan, S. S.; Yamashita, E. The Q cycle of cytochrome bc complexes: A structure perspective. *Biochim. Biophys. Acta, Bioenerg.* **2011**, *1807*, 788−802.
(43) Solomon, E. I.; Heppner, D. E.; Johnston, E. M.; Ginsbach, J. W.; Cirera, J.; Qayyum, M.; Kieber-Emmons, M. T.; Kjaergaard, C. H.; Hadt, R. G.; Tian, L. Copper Active Sites in Biology. *Chem. Rev.* **2014**, *114*, 3659−3853.
(44) Anson, C. W.; Ghosh, S.; Hammes-Schiffer, S.; Stahl, S. S. Co(salophen)-Catalyzed Aerobic Oxidation of p-Hydroquinone: Mechanism and Implications for Aerobic Oxidation Catalysis. *J. Am. Chem. Soc.* **2016**, *138*, 4186−4193.
(45) Becke, A. D. Density-functional exchange-energy approximation with correct asymptotic behavior. *Phys. Rev. A: At., Mol., Opt. Phys.* **1988**, *38*, 3098−3100.
(46) Becke, A. D. Density-functional thermochemistry. III. The role of exact exchange. *J. Chem. Phys.* **1993**, *98*, 5648−5652.
(47) Krishnan, R.; Binkley, J. S.; Seeger, R.; Pople, J. A. Self-consistent molecular orbital methods. XX. A basis set for correlated wave functions. *J. Chem. Phys.* **1980**, *72*, 650−654.
(48) Yan, J. J.; Kroll, T.; Baker, M. L.; Wilson, S. A.; Decréau, R.; Lundberg, M.; Sokaras, D.; Glatzel, P.; Hedman, B.; Hodgson, K. O.; Solomon, E. I. Resonant inelastic X-ray scattering determination of

https://dx.doi.org/10.1021/jacs.0c10385
J. Am. Chem. Soc. XXXX, XXX, XXX−XXX

the electronic structure of oxyhemoglobin and its model complex. *Proc. Natl. Acad. Sci. U. S. A.* **2019**, *116*, 2854.
(49) Han Du, W.-G.; Noodleman, L. Broken Symmetry DFT Calculations/Analysis for Oxidized and Reduced Dinuclear Center in Cytochrome c Oxidase: Relating Structures, Protonation States, Energies, and Mössbauer Properties in ba3 Thermus thermophilus. *Inorg. Chem.* **2015**, *54*, 7272−7290.
(50) Du, W.-G. H.; Götz, A. W.; Noodleman, L. DFT Fea3−O/O−O Vibrational Frequency Calculations over Catalytic Reaction Cycle States in the Dinuclear Center of Cytochrome c Oxidase. *Inorg. Chem.* **2019**, *58*, 13933−13944.
(51) Noodleman, L.; Case, D. A. Density-Functional Theory of Spin Polarization and Spin Coupling in Iron—Sulfur Clusters. In *Advances in Inorganic Chemistry;* Academic Press, 1992; Vol. *38*; pp 423−470. DOI: 10.1016/S0898-8838(08)60070-7
(52) Heinze, J.; Bard, A. J.; Faulkner, L. F. Electrochemical Methods−Fundamentals and Applications. *Ber. Bunsen-Ges.* **1981**, *85*, 1085−1086.
(53) Oliveira, R.; Zouari, W.; Herrero, C.; Banse, F.; Schöllhorn, B.; Fave, C.; Anxolabéhère-Mallart, E. Characterization and Subsequent Reactivity of an Fe-Peroxo Porphyrin Generated by Electrochemical Reductive Activation of O2. *Inorg. Chem.* **2016**, *55*, 12204−12210.
(54) Mittra, K.; Chatterjee, S.; Samanta, S.; Dey, A. Selective 4e−/4H+ O2 Reduction by an Iron(tetraferrocenyl)Porphyrin Complex: From Proton Transfer Followed by Electron Transfer in Organic Solvent to Proton Coupled Electron Transfer in Aqueous Medium. *Inorg. Chem.* **2013**, *52*, 14317−14325.
(55) Chatterjee, S.; Sengupta, K.; Mondal, B.; Dey, S.; Dey, A. Factors Determining the Rate and Selectivity of 4e−/4H+ Electrocatalytic Reduction of Dioxygen by Iron Porphyrin Complexes. *Acc. Chem. Res.* **2017**, *50*, 1744−1753.
(56) Chidsey, C. E. D. Free Energy and Temperature Dependence of Electron Transfer at the Metal-Electrolyte Interface. *Science* **1991**, *251*, 919.
(57) Mittra, K.; Chatterjee, S.; Samanta, S.; Sengupta, K.; Bhattacharjee, H.; Dey, A. A hydrogen bond scaffold supported synthetic heme FeIII−O2− adduct. *Chem. Commun.* **2012**, *48*, 10535−10537.
(58) Liu, J.-G.; Shimizu, Y.; Ohta, T.; Naruta, Y. Formation of an End-On Ferric Peroxo Intermediate upon One-Electron Reduction of a Ferric Superoxo Heme. *J. Am. Chem. Soc.* **2010**, *132*, 3672−3673.
(59) Liu, J.-G.; Ohta, T.; Yamaguchi, S.; Ogura, T.; Sakamoto, S.; Maeda, Y.; Naruta, Y. Spectroscopic Characterization of a Hydroperoxo−Heme Intermediate: Conversion of a Side-On Peroxo to an End-On Hydroperoxo Complex. *Angew. Chem., Int. Ed.* **2009**, *48*, 9262−9267.
(60) Kitagishi, H.; Tamaki, M.; Ueda, T.; Hirota, S.; Ohta, T.; Naruta, Y.; Kano, K. Oxoferryl Porphyrin/Hydrogen Peroxide System Whose Behavior is Equivalent to Hydroperoxoferric Porphyrin. *J. Am. Chem. Soc.* **2010**, *132*, 16730−16732.
(61) Tajima, K.; Shigematsu, M.; Jinno, J.; Ishizu, K.; Ohya-Nishiguchi, H. Generation of FeOEP-hydrogen peroxide complex (OEP = octaethylporphyrinato) by reduction of FeOEP−O2 with ascorbic acid sodium salt. *J. Chem. Soc., Chem. Commun.* **1990**, 144−145.
(62) Singha, A.; Mittra, K.; Dey, A. Effect of hydrogen bonding on innocent and non-innocent axial ligands bound to iron porphyrins. *Dalton Transactions* **2019**, *48*, 7179−7186.
(63) Nagaraju, P.; Ohta, T.; Liu, J.-G.; Ogura, T.; Naruta, Y. The secondary coordination sphere controlled reactivity of a ferric-superoxo heme: unexpected conversion to a ferric hydroperoxo intermediate by reaction with a high-spin ferrous heme. *Chem. Commun.* **2016**, *52*, 7213−7216.
(64) Ségaud, N.; Anxolabéhère-Mallart, E.; Sénéchal-David, K.; Acosta-Rueda, L.; Robert, M.; Banse, F. Electrochemical study of a nonheme Fe(ii) complex in the presence of dioxygen. Insights into the reductive activation of O2 at Fe(ii) centers. *Chemical Science* **2015**, *6*, 639−647.
(65) Warren, J. J.; Tronic, T. A.; Mayer, J. M. Thermochemistry of Proton-Coupled Electron Transfer Reagents and its Implications. *Chem. Rev.* **2010**, *110*, 6961−7001.
(66) Li, C.; Hoffman, M. Z. One-Electron Redox Potentials of Phenols in Aqueous Solution. *J. Phys. Chem. B* **1999**, *103*, 6653−6656.
(67) Hatcher, E.; Soudackov, A. V.; Hammes-Schiffer, S. Proton-Coupled Electron Transfer in Soybean Lipoxygenase. *J. Am. Chem. Soc.* **2004**, *126*, 5763−5775.
(68) Zhou, Z.; Khan, S. U. M. Inner-sphere reorganization energy of ions in solution: a molecular orbital calculation. *J. Phys. Chem.* **1989**, *93*, 5292−5295.

https://dx.doi.org/10.1021/jacs.0c10385
J. Am. Chem. Soc. XXXX, XXX, XXX−XXX